EUROPEAN ORGANIZATION FOR NUCLEAR RESEARCH
European Laboratory for Particle Physics

Large Hadron Collider Project

LHC Project Report 465

BEAM DUMPS AND BEAM STOPPERS FOR LHC AND CNGS TRANSFER LINES

S.Péraire and P.R. Sala

Abstract

Three new beam transfer lines are presently under construction at the SPS: TI2 and TI8 which will transfer protons and ions to the LHC, and TT41 which will transfer protons to the CNGS neutrino target. Three beam dumps (TED) and two beam stoppers (TBSE) will be installed in TI2 and TI8, and one TBSE in TT41. Both types of equipment are required to intercept the 450 GeV SPS beams concentrated in very short pulses (7.8 µs-10.5 µs) at intensities up to ~ 5 10^{13} protons, every 16.8 seconds for the TED and as single shot for the TBSE. The outer TED iron shielding will be identical to the existing SPS one, while dimensions and material composition of both TED and TBSE cores have been optimised to cope with the new beam conditions. The optimised TED inner core consists of a ∅80 mm graphite cylinder 2.9 m long, housed into a ∅80∕160 mm aluminium blind tube 3.5 m long, itself fitted into a ∅160∕310 mm copper blind tube 4.3 m long. The TBSE is made of the same graphite cylinder, housed into a ∅80∕120 mm aluminium blind tube 3.5 m long, itself fitted into a ∅120∕240 mm iron blind tube 4 m long. The maximum allowed beam intensity for a safe operation is given as a function of the pulse duration, including slow pulses as presently aborted on SPS dumps. The analytical methods set out in the thermo-mechanical part of this study are of general application, and may help in many other axi-symmetrical beam deposition analyses.

SL-BT

Contents

List of Tables

List of Figures

1. Introduction

Three new beam transfer lines are presently under construction at CERN. TI2 and TI8 will inject SPS beams into LHC, while TT41 will transfer protons extracted from SPS to the CNGS neutrino target.

Three beam dumps (TED) and two beam stoppers (TBSE) will be installed in the LHC transfer lines [1]. As shown in Fig. 1, the TEDs will be located at the two ends of the TI8 tunnel and at the TI2 exit only, the existing TCC6 dump acting as upstream TED for TI2. The TBSEs will stand at the entry of the TI2 and TI8 tunnels. Both types of equipment are required to intercept the 450 GeV SPS beam concentrated in very short pulses (7.8 μs for LHC), at intensities up to ~ $5\,10^{13}$ protons every 16.8 seconds. This value corresponds to the ultimate foreseen intensity according to the new 72 bunch scheme in the PS [3], and represents a ~ 20 % increase with respect to the intensity assumed as reference at the beginning of the TED optimisation [2]. The dumps should withstand these conditions for several hours, e.g. during extraction setting up. The stoppers, dedicated to personal safety, are supposed to absorb single pulses only occasionally (ideally never).

The new TED are the natural evolution of the existing ones, placed in TT20 and TT60 [4]. The existing TED's outer iron shielding will, wherever possible, be reused, while the inner core of both TED and TBSE has to be optimised. The optimisation must take into account several parameters, such as the total energy containment, the neutron fluence in the surrounding area, the thermal stresses, costs, and mechanical feasibility.

A third TBSE is foreseen at the entry of the TT41 neutrino tunnel [5]; it will be identical to the LHC transfer lines ones. The CNGS beam will be absorbed in 10.5 μs. More generally, these new dumps and stoppers should be able to sustain any other present and foreseen 450 GeV beam dumping conditions, in order to standardise as much as possible these types of equipment.

2. Geometry

- Schematic views of the layout of the old and new TED are presented in Fig. 2a. The outer shielding is made of cast iron and consists of a cylindrical part of 960 mm diameter and a forward conical part ending with a diameter of 550 mm, for a total length of 4300 mm. This shield contains a cylindrical inner core of 310 mm outer diameter.

The old TED core is 450 mm longer than the shield, extending out of it in the backward direction where it is partially shielded by an aluminium cylinder. The core itself consists of three concentric cylinders, with different lengths. The innermost and shortest one is made of graphite (2500 cm length, 80 mm diameter) to withstand the high temperatures at the shower maximum, then follow an aluminium container (3500 cm length, 160 mm diameter) and a copper container (4300 mm length, 310 mm diameter), both water cooled.

The core of the new TED is supposed to be fully contained in the shield, and to maintain the same radial structure as the old one, while the longitudinal structure optimisation is one of the subjects of this study.

- Figure 2b shows schematic views of the layout of the old and new TBSE. The old stopper is a simple iron cylinder of 200 mm diameter and 4000 mm total length, without outer shielding or water cooling. The new design adopts the same structure as the TED core, with the copper part substituted by iron. The partial lengths and diameters have to be optimised.

3. Simulations of particle cascades

All the simulations have been performed with the 1999 version of the FLUKA code. Details of the code and of its performances can be found elsewhere [6]. The geometrical model is quite simple, being composed by cylindrical (and possibly conical) layers.

No attempt has been made to model the details of the cooling system that are not relevant to the present calculation. The beam is assumed to be monochromatic, with a radial size of $\sigma_r = 0.58$ mm. This conservative value is 15 % smaller than the minimum radial beam size at the various installation locations. All the Monte Carlo results are normalised to one incident proton. The statistical aspect has to be treated with care, since it is required to determine with good accuracy the energy deposition in small volumes around the beam centre at several (5 to 8) interaction lengths from the beam impact position. The bin size for energy deposition is dictated by the dimensions of the beam spot and by the widening of the shower at large depths. A radial dimension of 0.25 mm has been used for the first part of the dump, up to 200 cm, and a coarser bin of 1 mm radial size for the rest. The longitudinal bin size is 2 cm in both cases. Transport thresholds have been set at 100 keV for electrons and 10 keV for photons in the scoring regions. Leading particle biasing has been applied up to 200 cm in graphite, and particle splitting biasing has been used at larger depths. The energy deposition in the first graphite layer has been evaluated in an unbiased run. The maximum temperature rise in the different materials has been calculated as a first guess in the adiabatic approximation for a single beam pulse, assuming the maximal beam intensity. For optimised configurations steady state analyses have been performed (see section 5.2.2). In all cases, the variation of the specific heat with temperature has been taken into account. Particles escaping from the dump have been recorded with boundary crossing estimators. The particle fluence around the dump has been calculated with track length estimators in the surrounding air. A box of 2×2×8 metres has been chosen as reference volume for the track length estimators.

4. Optimisation

The first choice of the dump composition and segmentation comes from the balance between temperature resistance and energy containment. In the case of a narrow beam, the maximum of the deposited energy density is located in a narrow zone along the beam axis at relatively small depth (about 10-20 cm for a 450 GeV beam in graphite). The relative values of this maximum in materials, when expressed in energy per unit of mass, scales more than linearly with the material density [7]. It is thus convenient to have light materials in the first layers of the dump to keep the temperature low. On the other hand, heavy materials are more effective in stopping the beam, and are used in the downstream sections of the dump. Thermo-mechanical properties and price also enter in the material choice. The most frequently used materials are graphite, aluminium, copper, iron and tungsten (see Table 1).

The total length of the dump is best described in terms of interaction lengths λ. The total attenuation of the primary beam depends exponentially on the number of interaction lengths in the dump. The density of deposited energy along the dump follows the development of the cascade, with an initial rise due to the production of secondary particles, each of which deposits part of its energy by ionisation, and generates further secondaries in inelastic interactions. A decrease in deposited energy follows when charged particles start to be rapidly absorbed without further reinteractions, that is as soon as their range becomes comparable to the inelastic interaction length. From this point on, an approximately exponential decrease is expected, following the propagation of the surviving fast hadrons. Figure 3 shows the fraction of energy deposited in the TED as a function of its length, up to 13.8 λ. About 80 % of the beam energy is already deposited after 6 radiation lengths (less than 3 metres of graphite, for

instance), while the last radiation length of material absorbs only 1 % of the energy. The curve of Fig. 3 converges asymptotically to a value that is smaller than 100 %, for several reasons :

- 1.1 % of the energy escapes laterally (~ 5 GeV)
- 4.7 % is lost in nuclear reactions, due to differences in binding energies (~ 21 GeV)
- 1.1 % is carried away by neutrinos (~ 5 GeV)

For all TED configurations considered, the energy deposited in the dump is about 92 % of the total, and only 1.3-1.7 % (6-7 GeV) is carried away by particles other than ν.

Neutrons, which are not slowed down by ionisation, form the majority of escaping particles, as can be seen in Table 2. Neutron spectra in the forward direction and from the sides are shown in Fig. 4. Most of the energy is carried out by neutrons below 10 MeV, and the typical evaporation peak around 1 MeV is clearly visible. The forward spectrum is slightly harder, as expected.

Escaping neutrons are the main contributors to the activation of the surrounding air, equipment and tunnel walls. They are slowed down by elastic interactions, which diffuse them in all directions, as seen in Fig. 5. At the end of their path, they undergo inelastic nuclear interactions, thus possibly producing radioactive isotopes. This is of particular concern in the case of repetitive beam dumping, with a consequent accumulation of radioactivity.

4.1 Dimensions

• The new TED design proposes a simplification of the dump geometry, with the elimination of the backward extrusion of the core. As a consequence the core will be reduced by 45 cm in length, which corresponds, if the material layering remains unchanged, to a reduction from the original 16.4 λ to 13.1 λ.

Since, as explained in the previous paragraph, the TED length is near to saturation and most of the energy escapes from the side, the expected impact on the energy containment is rather small. On the other hand, the relatively unshielded backward part of the old TED is likely to be a dangerous neutron source. FLUKA simulations, as reported in Table 3, predict an escaping energy of 6.0 ± 0.2 GeV (1.3 % of the beam energy) in the old configuration, and of 6.7 ± 0.3 GeV (1.5 % of the beam energy) in the new one. Conversely, the integrated hadron track length around the dump decreases from 56000 cm to 53600 cm. Neutron fluence in and around the dump for the old and new design are showed in Fig. 5. As already stated, the largest contribution comes from the sides. The enhancement of the backward flux in the old configuration is also visible.

These results, combined with the possibility of further optimisation and with the mechanical convenience, justify the choice of the new design.

Space constraints in the tunnels suggested the investigation of a possible reduction of the outer dump diameter. A calculation with an iron shield of 76 cm diameter predicts 10.7 ± 0.5 GeV of escaping energy and 86100 cm of neutron track length. That means a 60 % increase in both quantities and, therefore, a far less efficient beam dump regardless of intensity or frequency of the beam aborts (Fig. 5).

• The new TBSE is subject to space constraints that limit its total length to 4000 mm and its outside diameter to 240 mm. The graphite and aluminium parts of its core have the same length and diameter as in the new TED.

4.2 Material composition

All the numerical values reported in the following are consistent with the last adopted LHC filling scheme, which foresees a SPS proton cycle of either 3 or 4 PS batches of 72 bunches each. This scheme leads to an ultimate possible intensity of $4.9\,10^{13}$ protons per SPS cycle. However, the optimisation was performed on the basis of the old filling scheme, where each SPS cycle was supposed to contain 3 PS batches of 81 bunches each, for a total (ultimate) intensity of $4.13\,10^{13}$ protons. The ~20 % change in design intensity is reflected almost linearly on the expected temperatures in the dumps and stoppers. Fortunately, this rise, although non-negligible, remains within the safety margins adopted in the optimisation procedure.

- The TED must be able to sustain many beam aborts at the full intensity of $4.9\,10^{13}$ protons, without alteration of the properties of the core. Since the core itself has no structural function, steady state temperatures around 200 °C can be safely attained in aluminium, and 300 °C in copper. During the optimisation stage, only peak adiabatic temperatures have been calculated, aiming to remain even below the limits normally assumed for total mechanical integrity, that is 150 °C in aluminium and 220 °C in copper. Steady state calculations have been performed for optimised configurations.

Due to the smallness of the beam spot, the maximum attained energy density in graphite is quite high, i.e. $2.33\,10^{-11}$ J/g per proton, which corresponds to an increase in temperature of 800°C for the full beam intensity. Though this value is not critical, an analysis of the mechanical resistance to the thermal stress should be performed, notably because of the ensuing strong thermal gradient.

The starting point for the optimisation of the core material distribution was the old structure: 250 cm of graphite, 100 cm of aluminium and the remaining 80 cm of copper. As shown in Table 4, the original length of 250 cm of graphite is not enough to protect the downstream aluminium from overheating: an adiabatic increase of 210 °C of the temperature is expected within a 1 mm radius around the beam axis at about 10 cm depth in the aluminium layer. The energy deposition in copper is, however, well below the threshold.

The amount of graphite has therefore to be increased and the amount of aluminium can be reduced. As a first guess, it can be assumed that the peak energy density in aluminium after a given graphite length is proportional to the energy density at the same depth in a full graphite dump. The deposited energy density around the beam axis for a 350 cm long graphite dump is plotted in Fig. 6. Assuming an approximate linearity between energy and temperature, about 300 cm of graphite are needed to reduce to one half the aluminium heating. The Monte Carlo simulations confirm the proportionality assumption, with a ratio of aluminium/graphite of about 1.35, as seen from the values reported in Fig. 6.

On the same figure are also plotted the values of energy density deposited in a copper layer placed immediately after a graphite one. The proportionality still holds, but with a higher factor. The temperature increase in copper, after 300 cm of graphite, is as high as 710 °C for the full beam intensity. To go below 200 °C, more than 350 cm of graphite would be necessary (Table 4).

- The TBSE has less stringent requirements than the TED. Since it is expected to receive only single beam aborts, only adiabatic temperatures have to be taken into account, and no cooling is needed. However, an iron beam stopper could never sustain the ultimate beam intensity. The energy deposition per proton would attain $2.7\,10^{-10}$ J/g, thus already a beam intensity of about $3.7\,10^{12}$ protons would produce a local melting of the iron stopper (1540 °C). The same sandwich structure as in the new TED core has been adopted for the TBSE.

The copper sections have been replaced by iron, for cost and technical reasons. Since copper and iron have very close density, atomic number and specific heats, the considerations exposed above also apply to the TBSE.

4.3 Results

4.3.1 Dump

Several configurations have been tested, as shown in Tables 3 and 4. A plot of the escaping energy as a function of the number of radiation lengths in the dump is shown in Fig. 7. The considerations exposed above are confirmed by this plot. As an exercise, to enhance the lateral containment, the aluminium shell that surrounds the graphite was substituted by copper; the gain in efficiency is quite small.

The chosen design, which ensures acceptable temperatures in the core and a sufficient number of radiation lengths, consists of 290 cm of graphite, followed by 60 cm of aluminium and 80 cm of copper. A small increase of the dump containment could be achieved by adding a piece of tungsten at the end of the dump, but this small advantage is counterbalanced by the increase in cost, mechanical complexity and by the increase in the neutron fluence due to neutron multiplication in tungsten.

The longitudinal profile of the deposited energy density along the beam axis is shown in Fig. 8. The transitions between different materials are clearly visible. The maximum of this density occurs at 10 cm depth in aluminium and 5 cm depth in copper.

Radial profiles at the depth corresponding to the maximum are plotted in Figs 9 and 10. The peak of the energy density in graphite occurs at the very beginning of the cascade, where the secondary particles are still confined in a narrow cone around the primary direction. The cascade maximum is situated much deeper in the dump, and extends to the whole core, as shown in Fig. 12.

At the ultimate beam intensity, the adiabatic maximal temperature increases are 800°C in graphite, 130 °C in aluminium and 165 °C in copper. Temperatures drop rapidly away from the beam axis, as shown in Fig. 13. As can be seen from the values in Tables 3 and 4, only 1.5 % of the beam energy will escape from the optimised TED, i.e. almost the same as in the old configuration (1.3 %). The graphite core absorbs 21.9 % of the beam energy, while aluminium, copper and iron absorb 20.5 %, 36.1 % and 13.1 % respectively.

4.3.2 Stopper

The longitudinal material composition of the TBSE follows the one of the TED: 290 cm of graphite, followed by 60 cm of aluminium, and by 50 cm of iron to reach the maximal allowed length, for a total of 10.5 interaction lengths. The curve of Fig. 3 indicates that this should ensure a sufficient longitudinal containment. For obvious standardisation reasons, also the diameters of the graphite and aluminium cylinders have initially been kept equal to those of the TED core, that is a diameter of 80 mm of graphite, then aluminium up to 160 mm and the external iron jacket up to 240 mm. This, however, results in a poor lateral containment: as seen in Table 5, the escaping energy is 24 % of the beam energy, to be compared to 17 % in the old configuration. Most of this escapes from the sides: 104 GeV vs. the 4.5 GeV escaping from the front. A better efficiency is achieved by increasing the external iron thickness and reducing the aluminium one. An aluminium cylinder is anyhow necessary because of the fabrication procedure. In the final design, the 80 mm diameter graphite cylinder is surrounded by aluminium up to a 120 mm diameter and by iron up to 240 mm.

The peak of energy deposition in iron is very close to the front; the corresponding radial energy density distribution is plotted in Fig. 11. The maximum temperature increase is about 130 °C in the iron front, and only 15 °C on the side.

The escaping energy is 20 % of the total; this represents a good compromise between energy containment, temperature resistance and space constraints. Aluminium and iron absorb 16.7 % and 36.3 % of the beam energy respectively.

5. Thermo-mechanical analysis

Two beam dumps and one beam stopper are presently in use in the SPS transfer lines TT20 and TT60. Most of the pulses they have to intercept are relatively slow (of the order of milliseconds to seconds). In order to make the new LHC dumps as polyvalent as possible, it would be an advantage that they could also withstand very high beam intensities 'slowly' dumped. Two types of 450 GeV beam, of radial size $\sigma_r = 0.58$ mm, are consequently considered here :

- $5 \, 10^{13}$ protons dumped in 6 μs,
- $7 \, 10^{13}$ protons dumped in 1.5 s (this hypothetical intensity being greatly above the present possibilities of the PS-SPS complex),

with 16.8 s repetition period on the TED and as a single shot on the TBSE.

The ultimate goal of this study is to define the maximum allowed beam intensity as a function of the pulse duration, for beam energies, beam sizes and repetition periods close to the above nominal values.

5.1 General assumptions

Several 1D analytical models are used to perform the successive steps of this thermo-mechanical analysis :

- 1D axi-symmetrical models (radius r dependant), to estimate transient temperatures, quasi-static and radial dynamic stresses,
- 1D Cartesian model (axial co-ordinate z dependant), to estimate longitudinal dynamic stresses.

The stresses remain in the elastic domain where Hooke's law applies, and the small strain approximation is supposed to hold.

Generalised plane strain (plane sections remain plane) is assumed, with free radial expansion for aluminium, copper and iron, and prevented radial expansion for graphite (thermally shrink fitted into aluminium). Equations and analytical solutions are developed below; all are time t dependant.

The radial energy density $d(r)$ and instantaneous temperature rise $\Delta T(r)$ are assumed to be uniform along the z axis of the solid cylinder. To perform the transient thermal analysis, a Gaussian distribution is adopted :

$$d(r) = d_0 \cdot \exp(-b_d \cdot r^2) \qquad \forall z \qquad (1a)$$

$$\Delta T(r) = \Delta T_0 \cdot \exp(-b_T \cdot r^2) \qquad \forall z \qquad (1b)$$

d_0 and b_d being estimated in such a way that the Gaussian distribution has the same maximum and radial integral as the original one (d_0, b_d, ΔT_0 and b_T are listed in Table 6). Other than defined in the text, the symbols and units used in this section are defined in Tables 1 and 7.

The temperature rise ΔT from an initial temperature T_i is derived from the volumic energy d, by means of the relation :

$$d = \rho \cdot \int_{T_i}^{T_i + \Delta T} C_p(T) \cdot dT \tag{2}$$

$d(r)$ and $\Delta T(r)$, induced by $7\ 10^{13}$ protons at 450 GeV, are displayed in Figs 14 for the four materials.

Whatever the cooling system used (forced water or natural air convection), a thermal exchange is defined at the surface of the cylinder by the *cooling factor h* [11]:

$$h(cm^{-1}) = \frac{\text{coolant heat transfer coefficient}}{\text{material thermal conductivity}} = \frac{k_e\ (W/cm^2 \cdot {}^\circ C)}{\lambda\ (W/cm \cdot {}^\circ C)} \tag{3}$$

All materials are assumed to be homogeneous and isotropic. Their thermal and mechanical properties are temperature T ($^\circ K$) dependant. See Tables 1 and 7 for room temperature values, and Figs 15 for temperature evolution [8, 9]. All these functions fit the relation :

$$F(T) = F(293) \cdot \left[1 + k_1 \cdot (T - 293) + k_2 \cdot (\frac{1}{T^2} - \frac{1}{293^2}) \right] \tag{4}$$

The Von Mises strength criterion σ_{eq} is applied to estimate the resistance of metallic materials with the same tensile and compressive yield limit ($\sigma_{0,2}$), while the Stassi criterion σ_{teq} is used to assess the resistance of graphite which has differing tensile (σ_0) and compressive (σ_0') strength limits [10] :

$$\sigma_{eq}^2 = \sigma_r^2 + \sigma_\theta^2 + \sigma_z^2 - \sigma_r . \sigma_\theta - \sigma_r . \sigma_z - \sigma_\theta . \sigma_z \tag{5a}$$

$$k_s \cdot \sigma_{teq}^2 - (k_s - 1) \cdot (\sigma_r + \sigma_\theta + \sigma_z) \cdot \sigma_{teq} - \sigma_{eq}^2 = 0 \tag{5b}$$

σ_r, σ_θ and σ_z being the principal stresses in cylindrical co-ordinates, and $k_s = \sigma_0'/\sigma_0 \geq 1$. Note that the two criteria become identical if $k_s = 1$.

5.2   Thermal history

A full thermal history involves two successive studies :

-    single shot transient analysis, down to a quasi-uniform temperature distribution close to the initial one T_i ,

-    steady state analysis, by superposition of successive pulses.

5.2.1 Single shot

An infinite cylinder of radius R is subjected to a heat load H(t) resulting in an initial axi-symmetrical Gaussian heating ΔT_h :

$$\Delta T_h(r,t) = \Delta T_0 \cdot \exp(-b \cdot r^2) \cdot \int_0^t H(t) \cdot dt \tag{6}$$

Its temperature evolves in time according to Fouriers's equation and boundary condition

$$\frac{\partial T(r,t)}{\partial t} = a \cdot \left(\frac{\partial^2 T(r,t)}{\partial r^2} + \frac{1}{r} \cdot \frac{\partial T(r,t)}{\partial r} \right) + \frac{\partial T_h(r,t)}{\partial t} \tag{7a}$$

$$\frac{\partial T}{\partial r}(R,t) = -h \cdot \Delta T(R,t) \tag{7b}$$

- If the heating can be considered as instantaneous (pulse duration in the range of microseconds or less) H(t) becomes a Dirac function, and the solution of Eqs (7) is [11] :

$$\Delta T(r,t) = \frac{2\Delta T_0}{R^2} \sum_{n=1}^{\infty} \exp(-a\,\alpha_n^2 t)\ \frac{\alpha_n^2\,J_0(\alpha_n r)}{(h^2+\alpha_n^2)\,J_0^2(\alpha_n R)} \int_0^R r\,\exp(-br^2)\,J_0(\alpha_n r)\,dr \quad (8)$$

the infinite series α being all the positive solutions of

$$h \cdot J_0(\alpha_n R) - \alpha \cdot J_1(\alpha_n R) = 0 \quad\quad (9)$$

where J_0 and J_1 are Bessel functions of the first kind. In reality, the series is practically limited to its first 80 to 120 terms.

Even though the diffusivity a is assumed constant in Eq. (7a), it is actually strongly temperature dependant. To reduce this difficulty, a is iteratively adapted to the local temperature :

$$a(T_i) \rightarrow T_1 \rightarrow a(T_1) \rightarrow T_2 \rightarrow a(T_2) \ \dots\ \text{up to}\ |T_n\text{-}T_{n-1}| \leq 0.1\ °C$$

The on-axis initial temperature decrease rate is

$$\frac{\partial T}{\partial t}(0,0) = -4\,a\,b\,\Delta T_0 \quad\quad (10)$$

- In the event of progressive heating of duration t_0, H(t) is assumed to be a symmetric trapezoidal function defined over the interval [0, t_0], whose integral from 0 to t_0 is 1. The solution of Eqs (7) is then :

$$\Delta T(r,t) = \frac{2\Delta T_0}{R^2} \sum_{n=1}^{\infty} \int_0^t H(\theta)\,\exp[-a\,\alpha_n^2(t-\theta)]\,d\theta\ \frac{\alpha_n^2\,J_0(\alpha_n r)}{(h^2+\alpha_n^2)\,J_0^2(\alpha_n R)} \int_0^R r\,\exp(-br^2)\,J_0(\alpha_n r)\,dr \quad (11)$$

The H(t) rise and fall times are assumed to be 25 % of t_0 each, though they do not in practice last more than few milliseconds. H(t) has therefore a conservative maximum value.

Both (8) and (11) account for the three successive stages of this transient process :

- internal heat transfer only, by conduction in matter, in the absence of external thermal gradient: $\Delta T(R, t) = 0$,
- external cooling by convection at the surface of the cylinder (Eq. 7b), down to a quasi-uniform temperature distribution $\Delta T_u \approx \Delta T(r, t_u)\quad \forall r$,
- quasi-uniform exponential cooling of the whole cylinder :

$$\Delta T(r,t) \approx \Delta T_u \cdot \exp\left(\frac{t_u - t}{\tau}\right)\quad \forall r, \qquad \text{with}\quad \tau = \frac{R}{2\,a\,h} \quad\quad (12)$$

Figures 16 show the transient evolution of a 450 GeV single pulse of $5\ 10^{13}$ protons instantaneously hitting one of the four materials, graphite, aluminium, copper and iron respectively.

The temperature rise $\Delta T(t)$ is displayed for several radii, $r = 0$ and $r = R$ in particular. Table 8 (fast pulse) gives some typical figures for the process: ΔT_{max} is the on-axis initial temperature rise, t_ε is the time for ΔT_{max} to decrease by 1 % (it lies in the range of milliseconds, and justifies therefore the assumption of considering pulses in the range of microseconds as instantaneous), t_c is the time for external cooling to become effective ($\Delta T(R) \neq 0$), t_u is the time for the whole cylinder to reach a quasi-uniform exponential cooling with a tolerance of 1 % of ΔT_{max}. One can conclude that the various materials have very different behaviour under the

same beam conditions; graphite has the best diffusivity and cooling combination, iron has the worst.

Figures 17 and Table 8 (slow pulse) give similar information for a 450 GeV single pulse of $7\ 10^{13}$ protons dumped in $t_0 = 1.5$ seconds. The maximum on-axis temperature rise occurs at $t_{max} \approx 2/3$ of t_0. It is obviously lower than the related adiabatic ΔT_0 (see Table 6); 92 % of ΔT_0 for iron and only 17 % for graphite, for the reason mentioned above.

5.2.2 Steady state

The specific heat C_p being temperature dependant, it is more accurate to perform the pulse superposition in terms of energy density than in terms of temperature rise. $\Delta T(r, t)$ is therefore translated into $d(r,\theta)$, which is defined by Eq. (2) if $\theta \geq 0$ and vanishes if $\theta < 0$. The total energy density $\Sigma d(r, t)$, resulting from N successive pulses of repetition period t_p and defined in the time interval $[0, N \cdot t_p]$, is :

$$\Sigma d(r,t) = \sum_{n=1}^{N} d\left(r,\ t - (n - 1) \cdot t_p\right) \tag{13}$$

$\Sigma d(r, t)$ is in turn translated back to $\Sigma T(r, t)$ by Eq. (2), in such a way that the temperature resulting from N successive pulses be $T(r, t) = \Sigma T(r, t) + T_i$.

A steady state is reached after N_s pulses, when energy gained by heating is equal to energy lost by cooling . $T(r, t)$ becomes then periodic:

$$T(r,\ t + t_p) = T(r,\ t) \quad \forall t > N_s \cdot t_p. \tag{14}$$

Periodic thermal cycling of the three materials subjected to successive 6 µs pulses every $t_p = 16.8$ s is shown in Figs 18, while Figs 19 display the same history for pulses of 1.5 s duration. Table 9 gives some typical figures for both cases: τ is the time constant of exponential cooling reached at time t_u on the surface of the cylinder, T_{max} and T_{min} are the extreme on-axis steady state temperatures reached after N_s pulses, i.e. after a time $N_s \cdot t_p$.

For metallic materials, thermal cycling increases T_{max} by 25 % to 45 %, which corresponds to a rise of several tens of degrees, but remains acceptable for elements without any structural function: ~ 220 °C in aluminium and ~ 260 °C in copper. For graphite, T_{max} is practically not affected by thermal cycling. This maximum temperature of 860 °C is very modest compared to the possibilities of the material (up to 3000 °C in absence of oxygen). Note that, in spite of 40 % more beam intensity in the slow pulse, the maximum graphite temperature is about four times lower than for the fast pulse, thanks to progressive heating.

5.3 Quasi-static stresses

Fast and slow pulses have been distinguished in the frame of the above thermal analysis. They should also be distinguished - differently - in the frame of a mechanical analysis.

A fast pulse does not allow free thermal expansion of matter while it occurs, and therefore generates mechanical shock waves. Its duration is of the same order (or shorter) as the time spent by the waves to travel half of the minimum cylinder dimension. This time varies from ~ 15 µs (radial motion in aluminium) to ~ 110 µs (axial motion in copper).

One can conclude that 6 µs fast pulses generate radial and axial dynamic stresses into the four materials, while slow 1.5 s pulses only produce quasi-static stresses.

The principal quasi-static thermal stresses σ_r, σ_θ and σ_z induced in an infinite cylinder of radius R, by a radial temperature distribution $\Delta T(r, t)$ uniform along its axis, is [12, 13] :

- radial stress :

$$\sigma_r(r,t) = -\frac{1}{r^2}\int_0^r p(r,t) \cdot r \cdot dr + \frac{m}{R^2}\int_0^R p(r,t) \cdot r \cdot dr \qquad (15)$$

- tangential stress :

$$\sigma_\theta(r,t) = \frac{1}{r^2}\int_0^r p(r,t) \cdot r \cdot dr + \frac{m}{R^2}\int_0^R p(r,t) \cdot r \cdot dr - p(r,t) \qquad (16)$$

- longitudinal stress :

$$\sigma_z(r,t) = \frac{2n}{R^2}\int_0^R p(r,t) \cdot r \cdot dr - p(r,t) \qquad (17)$$

$$\text{where} \quad p(r,t) = \frac{E \cdot \alpha \cdot \Delta T}{1-\nu}(r,t) \qquad (18)$$

E and α being temperature dependant, and therefore functions of r and t, as is ΔT [1]. The coefficients m and n depend on the boundary conditions (radial and axial expansions); they are listed in Table 10 [2].

Generalised plane strain (indices a and c in Table 10), which implies free uniform axial expansion, is granted by computing the longitudinal stress σ_z as :

$$\sigma_z = \sigma_{z0} - \frac{2}{R^2}\int_0^R \sigma_{z0} \cdot r \cdot dr \qquad (19a)$$

$$\text{where} \quad \sigma_{z0} = \nu(\sigma_r + \sigma_\theta) - E \cdot \alpha \cdot \Delta T \qquad (19b)$$

σ_{z0} being the longitudinal stress produced by prevented axial expansion (indices b and d).

Figures 20 display, for the four materials, the time evolution of the principal quasi-static thermal stresses induced on-axis ($r = 0$) by a 1.5 s slow pulse of $7\,10^{13}$ protons. Expansion is free, except for graphite for which radial expansion is prevented. The initial temperature is T_{min} from Table 9 (periodic cycling of slow pulse), and 20 °C for iron. Starting from zero, these stresses later remain compressive. They reach an extreme amplitude at time t_{max} (Table 8), and then their absolute value drops more or less rapidly depending on the material: except for iron, they become negligible after $t_p = 16.8$ s. As $r = 0$, σ_r and σ_θ are identical and, for free radial expansion, equal to $\sigma_z/2$; if furthermore, $k_s = 1$, $\sigma_{teq} = \sigma_{eq} = |\sigma_z/2|$. The three metallic materials fulfil these two conditions. For each material, Table 11 gives the extreme amplitude of σ_r, σ_θ, σ_z and σ_{teq}, and the standard tensile strength limit σ_0 (= yield limit $\sigma_{0,2}$ for metallic material). This limit is far from being reached for graphite and aluminium ($\sigma_{teq} << \sigma_0$), but it is widely exceeded for copper and iron, prompting a search for more resistant alloys (σ_0 in brackets, see Table 16).

Figures 21 display the radial distribution of these same stresses at time t_{max}, and show that their extreme amplitude is located on-axis. For the three metallic materials, $\sigma_\theta(R) = \sigma_z(R) = \sigma_{eq}(R) > 0$ and $\sigma_r(R) = 0$. For graphite, $\sigma_r(R) < 0$, as its radial expansion is prevented.

---

[1] Contrary to [12] and [13] where E is assumed to be constant.

[2] Note an erroneous value of m (index c) in the first edition of [13].

To conclude this quasi-static analysis, standard graphite and aluminium easily withstand a periodic cycling of $7\,10^{13}$ protons dumped in 1.5 s every 16.8 s, while copper and iron do not. For this latter, a more resistant alloy should be used. As it would be too expensive to replace all the copper part, a 25 cm short cylinder $\varnothing$5.8 cm, made of special Cu alloy, will be thermally shrink fitted into the upstream part of the standard copper block, where σ_{eq} should remain $\leq$ 70 MPa. From this point of the study, the radius of the copper cylinder is assumed to be R = 2.9 cm instead of 15.5 cm as previously.

5.4 Dynamic stresses

As already mentioned in the previous section, a 6 μs fast pulse does not allow free thermal expansion of matter while it occurs. Radial and longitudinal mechanical shock waves are therefore generated, whose initial states should be defined first. They then are separately analysed before being combined. Both analyses are performed by solving a differential equation of motion of the functions u(r, t) and w(z, t) respectively :

- u(r, t) is the radial displacement of a cylindrical surface from equilibrium,

- w(z, t) is the axial displacement of a plane section from equilibrium.

These displacements are linked to σ_r, σ_θ and σ_z by Hooke's law, via the principal strains ε_r, ε_θ and ε_z :

$$\varepsilon_r = \frac{1}{E}\left[\sigma_r - \nu\left(\sigma_\theta + \sigma_z\right)\right] + \alpha \cdot \Delta T \tag{20a}$$

$$\varepsilon_\theta = \frac{1}{E}\left[\sigma_\theta - \nu\left(\sigma_r + \sigma_z\right)\right] + \alpha \cdot \Delta T \tag{20b}$$

$$\varepsilon_z = \frac{1}{E}\left[\sigma_z - \nu\left(\sigma_r + \sigma_\theta\right)\right] + \alpha \cdot \Delta T \tag{20c}$$

and

$$\frac{\partial u}{\partial r}(r,t) = \varepsilon_r(r,t) \tag{21a}$$

$$u(r,\,t) = r \cdot \varepsilon_\theta(r,\,t) \tag{21b}$$

$$w(z,\,t) = z \cdot \varepsilon_z(t) \tag{21c}$$

5.4.1 Initial conditions

The initial radial and axial displacements are obtained by changing the sign of the quasi-static displacements produced by the instantaneous temperature rise $\Delta T_i(r)$ given by simulation of particle cascade (note that the Gaussian approximation of Eq. (1b) is no longer used) :

$$p_i(r) = \frac{E \cdot \alpha \cdot \Delta T_i(r)}{1 - \nu} \rightarrow \sigma_{ri}(r), \sigma_{\theta i}(r), \sigma_{zi}(r) \rightarrow u_i(r), w_i(z) \ ,$$

they are therefore equal to $-u_i(r)$ and $-w_i(z)$ respectively.

Figures 22 display, for the four materials, the radial distribution of the quasi-static stresses $\sigma_{ri}(r)$, $\sigma_{\theta i}(r)$ and $\sigma_{zi}(r)$ generated by a 6 μs fast pulse of $5\,10^{13}$ protons. These stresses are important to know, as they are the mean values around which the dynamic stresses oscillate. Their extreme amplitude is located on-axis, as for Figs 21. The corresponding radial displacement $u_i(r)$ is also displayed. With the axial displacement $w_i(z)$, these functions define the initial state of the dynamic stresses. Their extreme amplitude is listed in Table 12: $u_{i\ max}$ is

the maximum value of $u_i(r)$ and $w_{i\,max} = w_i(L)$ is the maximum value of $w_i(z)$, L being the half length of the cylinder.

5.4.2 Radial stresses

A long cylinder of radius R, subjected to an initial radial displacement $-u_i(r)$, sustains a transverse mechanical shock wave whose differential equation of motion is [13]:

$$\frac{\partial^2 u}{\partial t^2} = c_r^2 \cdot \left(\frac{\partial^2 u}{\partial r^2} + \frac{1}{r} \cdot \frac{\partial u}{\partial r} - \frac{u}{r^2} \right) \tag{22a}$$

c_r being proportional to the velocity of sound c :

$$c_r^2 = \frac{1-\nu}{(1+\nu)(1-2\nu)} \cdot c^2 \tag{22b}$$

- If $-u_i(r)$ is instantaneously applied, the general solution of Eq. (22a) is :

$$\varepsilon_r(r,t) = \frac{\partial u}{\partial r}(r,t) = -u_{i\,max} \sum_{n=1}^{\infty} \beta_n \left(\alpha_n \, J_0(\alpha_n r) - \frac{1}{r} J_1(\alpha_n r) \right) \cos\left(c_r \alpha_n t\right) \tag{23a}$$

$$r \cdot \varepsilon_\theta(r,t) = u(r,t) = -u_{i\,max} \sum_{n=1}^{\infty} \beta_n \, J_1(\alpha_n r) \, \cos\left(c_r \alpha_n t\right) \tag{23b}$$

and generalised plane strain is obtained by adding a uniform longitudinal strain derived from equations similar to (19) :

$$\varepsilon_z(t) = \frac{w(z,t)}{z} = -\frac{2\nu}{1-\nu} \frac{u(R,t)}{R} \tag{23c}$$

This superposition of stress states obviously vanishes if $u(R,\ t) = 0$, and does not introduce extra σ_r nor σ_θ stresses if radial expansion is free. The general expression of the principal dynamic stresses is then obtained by inverting Hooke's law :

$$\sigma_r = \frac{E}{(1+\nu)(1-2\nu)} \left[\nu \frac{u}{r} + (1-\nu) \frac{\partial u}{\partial r} \right] \tag{24a}$$

$$\sigma_\theta = \frac{E}{(1+\nu)(1-2\nu)} \left[(1-\nu) \frac{u}{r} + \nu \frac{\partial u}{\partial r} \right] \tag{24b}$$

$$\sigma_z = \frac{\nu E}{(1+\nu)(1-2\nu)} \left[\frac{u}{r} + \frac{\partial u}{\partial r} - 2 \frac{u(R)}{R} \right] \tag{24c}$$

The infinite series α and β in (23a) and (23b) are defined by the boundary and initial conditions respectively, as follows :

5.4.2.1 Boundary conditions :
- free radial expansion :

$\sigma_r(R,t) \div \sum_{n=1}^{\infty} \beta_n \left((1-\nu)\, \alpha_n \cdot J_0(\alpha_n R) - \frac{1-2\nu}{R} \cdot J_1(\alpha_n R) \right) \cos\left(c_r \alpha_n t\right) = 0$, if α represents all the

positive solutions of:

$$(1-\nu)\, \alpha_n \cdot J_0(\alpha_n R) - \frac{1-2\nu}{R} \cdot J_1(\alpha_n R) = 0 \tag{25a}$$

- prevented radial expansion :

$$u(R,t) \div \sum_{n=1}^{\infty} \beta_n \, J_1(\alpha_n R) \cos(c_r \alpha_n t) = 0, \text{ if } \alpha \text{ represents all the positive solutions of :}$$

$$J_1(\alpha_n R) = 0 \qquad (25b)$$

Note that $u(R) = 0$ implies that $\varepsilon_z = 0$ and vice versa. That means that only two boundary states are possible: either complete free expansion $(\sigma_r(R) = 0$ and $\varepsilon_z = C^t)$ or complete prevented expansion $(u(R) = 0$ and $\varepsilon_z = 0)$, but not mixed free and prevented expansions as for quasi-static states.

5.4.2.2 Initial conditions :

$$u(r,0) = -u_{i\,max} \sum_{n=1}^{\infty} \beta_n \, J_1(\alpha_n r) = -u_i(r), \text{ if } \beta \text{ represents all the positive solutions of :}$$

$$\frac{u_i(r)}{u_{i\,max}} = \sum_{n=1}^{\infty} \beta_n \, J_1(\alpha_n r) \quad \forall r \qquad (26)$$

β depends therefore on α, and Eq. (26) should be satisfied for any value of r. In practice, α and β have the same number of terms (n = 80 to 120), α is computed first by means of one of the Eqs (25) and then β is obtained by solving a linear system of n equations corresponding to n equidistant values of $r \neq 0$. The terms β_n are dimensionless, while the terms α_n have the dimension L^{-1} as in section 5.2.1.

On-axis the radial and tangential stresses are identical :

$$\sigma_r(0,t) = \sigma_\theta(0,t) = \frac{-E\,u_{i\,max}}{2(1+\nu)(1-2\nu)} \sum_{n=1}^{\infty} \alpha_n \beta_n \cos(c_r \alpha_n t) \qquad (27a)$$

and

$$\sigma_z(0,t) = \frac{-\nu\,E\,u_{i\,max}}{(1+\nu)(1-2\nu)} \sum_{n=1}^{\infty} \beta_n \left(\alpha_n - \frac{2}{R} J_1(\alpha_n R) \right) \cos(c_r \alpha_n t) \qquad (27b)$$

As σ_r and σ_θ are strongly dependent on $J_1(\alpha_n r)/r$, they rapidly drop when r increases, so that their extreme values are located on-axis.

In order to compare with real fast pulses of finite duration, a theoretical instantaneous pulse of $5\,10^{13}$ protons has been applied to the four materials. The time evolution of the principal dynamic stresses thus generated on-axis are displayed in Figs 23, and their minimum and maximum values are listed in Table 13.

- If the initial displacement is progressively applied with a constant gradient $-u_i(r)/t_0$, $u(r, t)$ should satisfy the equation :

$$u(r,t) = \frac{1}{t_0} \int_0^{t_0} u_{i\,instant.}(r,t-\theta)\,d\theta \qquad (28)$$

$u_{instant.}$ being given by Eq. (23b). The general solution of Eq. (28) is :

$$\frac{\partial u}{\partial r}(r,t) = \frac{-u_{i\,max}}{c_r t_0} \sum_{n=1}^{\infty} \beta_n \left(J_0(\alpha_n r) - \frac{1}{\alpha_n r} J_1(\alpha_n r) \right) [\sin(c_r \alpha_n t) - \sin(c_r \alpha_n (t-s))] \qquad (29a)$$

$$u(r,t) = \frac{-u_{i\,max}}{c_r t_0} \sum_{n=1}^{\infty} \frac{\beta_n}{\alpha_n} J_1(\alpha_n r) [\sin(c_r \alpha_n t) - \sin(c_r \alpha_n (t-s))] \qquad (29b)$$

with
$$s(t) = t \text{ if } t \le t_0 \text{ and } s(t) = t_0 \text{ if } t > t_0 \tag{30}$$

Beyond t_0, each function results from superposition of two identical periodic waves of opposite amplitude, shifted by t_0. On-axis the radial and tangential stresses are identical :

$$\sigma_r(0,t) = \sigma_\theta(0,t) = \frac{-E u_{i\,max}}{2(1+\nu)(1-2\nu)} \frac{1}{c_r t_0} \sum_{n=1}^{\infty} \beta_n \left[\sin(c_r \alpha_n t) - \sin(c_r \alpha_n (t-s)) \right] \tag{31a}$$

and $\sigma_z(0,t) = \dfrac{-\nu E u_{i\,max}}{(1+\nu)(1-2\nu)} \dfrac{1}{c_r t_0} \displaystyle\sum_{n=1}^{\infty} \dfrac{\beta_n}{\alpha_n} \left(\alpha_n - \dfrac{2}{R} J_1(\alpha_n R) \right) \left[\sin(c_r \alpha_n t) - \sin(c_r \alpha_n (t-s)) \right]$ (31b)

Figures 24 display, for the four materials, the time evolution of the principal dynamic stresses generated on-axis by a $6\,\mu s$ pulse of $5\,10^{13}$ protons. Table 13 lists their minimum and maximum values which may be compared with those of the instantaneous pulse: they are about ten times lower for graphite, and more than two times lower for the metallic materials. The pseudo-period t_r of these functions is also listed, according to the estimation proposed in [13]. This latter applies very well to aluminium ($38\,\mu s$) and copper ($19\,\mu s$), but not to graphite and iron whose pseudo-period is difficult to evaluate as their ratio t_0 / t_r is lower.

5.4.3 Axial stresses

A 2L long straight bar of constant cross-section (not necessary circular) subjected to an initial axial displacement $-w_i(z)$ uniform over the section, sustains a longitudinal mechanical shock wave whose equation of motion is [14]:

$$\frac{\partial^2 w}{\partial t^2} = c^2 \frac{\partial^2 w}{\partial z^2} \tag{32}$$

$z = 0$ being the middle of the bar, $w_i(0)$ is assumed to be zero because of symmetry.

- If $-w_i(z)$ is instantaneously applied, the general solution of Eq. (32) is :

$$\varepsilon_z(z,t) = \frac{\partial w}{\partial z}(z,t) = \frac{4}{\pi} \frac{w_{i\,max}}{L} \sum_{n=1}^{\infty} \frac{(-1)^n}{(2n-1)} \cos(\alpha_n z) \cos(c\,\alpha_n t) \tag{33a}$$

$$w(z,t) = \frac{8}{\pi^2} w_{i\,max} \sum_{n=1}^{\infty} \frac{(-1)^n}{(2n-1)^2} \sin(\alpha_n z) \cos(c\,\alpha_n t) \tag{33b}$$

with
$$\alpha_n = \frac{(2n-1)\pi}{2L} \tag{34}$$

The longitudinal stress $\sigma_z(z, t) = E \varepsilon_z(z, t)$ which propagates along the bar is, as $w(z, t)$, a periodic function of period $t_z = 4L /c$. It is discontinuous and takes successively in time the discrete values $\pm E w_{i\,max} /L$ or 0.

- If the initial displacement is progressively applied with a constant gradient $-w_i(z)/t_0$, $w(z, t)$ should satisfy the equation :

$$w(z,t) = \frac{1}{t_0} \int_0^{t_0} w_{instant.}(z, t - \theta)\, d\theta \tag{35}$$

$w_{instant.}$ being given by Eq. (33b). The general solution of Eq. (35) is :

$$w(z,t) = \frac{16L}{\pi^3} \frac{w_{i\,max}}{c\,t_0} \sum_{n=1}^{\infty} \frac{(-1)^n}{(2n-1)^3} \sin(\alpha_n z) \left[\sin(c\,\alpha_n t) - \sin(c\,\alpha_n (t-s)) \right] \tag{36a}$$

19

$$\sigma_z(z,t) = \frac{8}{\pi^2} \frac{E\, w_{i\,max}}{c\, t_0} \sum_{n=1}^{\infty} \frac{(-1)^n}{(2n-1)^2} \cos(\alpha_n z)\left[\sin(c\,\alpha_n t) - \sin(c\,\alpha_n (t-s))\right] \qquad (36b)$$

These periodic functions ($t_z = 4L/c$) result again from superposition of two identical periodic waves of opposite amplitude, shifted by t_0. For all the cases analysed, the extreme amplitude of σ_z is also $\pm E\, w_{i\,max}/L$ ($\forall z \neq L$), as the ratio $t_0/t_z < 0.5$ [13]. Figures 25 display, for the four materials, the time evolution of the axial dynamic stress generated in the middle of the bar by the longitudinal shock wave induced by a $6\,\mu s$ pulse of $5\,10^{13}$ protons. Table 14 lists its period t_z and its extreme amplitude; this latter is fairly high for copper ($\pm 87\,MPa$), modest for aluminium and iron ($\pm 20\,MPa$ and $\pm 13\,MPa$ respectively), and practically negligible for graphite ($\pm 0.2\,MPa$).

5.4.4 Total stresses

In absence of any damping, the total principal stresses result from the superposition of three components, i.e. the quasi-static component proportional to the *filling function* $f(t) = s(t)/t_0$ (see 30), and the two radial and axial dynamic components. Far enough away from the extremities of the cylinder, in such a way that plane section remains plane, they are :

$$\sigma_r(r,t) = \sigma_{ri}(r)\cdot f(t) + \sigma_{r\,radial}(r,t) \qquad (37a)$$

$$\sigma_\theta(r,t) = \sigma_{\theta i}(r)\cdot f(t) + \sigma_{\theta\,radial}(r,t) \qquad (37b)$$

$$\sigma_z(r,z,t) = \sigma_{zi}(r)\cdot f(t) + \sigma_{z\,radial}(r,t) + \sigma_{z\,axial}(z,t) \qquad (37c)$$

For the four materials, Figs 26 display the time evolution of the total stresses σ_r, σ_θ, σ_z and σ_{teq} generated at the centre of the cylinder ($r=0$, $z=0$) by the mechanical shock wave induced by a $6\,\mu s$ pulse of $5\,10^{13}$ protons. This location is selected because the radial dynamic stresses exhibit their extreme amplitudes at $r=0$, and the axial ones at any $z \neq L$. Starting from zero, each stress function later oscillates in time between two limits listed in Table 15. The maximum equivalent Stassi stress σ_{teq} has to be compared to the tensile strength limit σ_0 recorded in Table 11. Higher than that produced by a slow pulse, σ_{teq} remains negligible for graphite, but is not acceptable for any standard aluminium, copper nor iron. More resistant alloys should therefore be used (see Table 16). Moreover, such mechanical waves induce fatigue phenomena; Figs 27 schematically display these vibrations in the Goodmann's chart of the selected aluminium and copper alloys. Assuming, as a conservative approximation, an alternating fatigue limit σ_f of about half the ultimate strength σ_R leads to an infinite life time for both alloys (fatigue is not a concern for TBSE). It should be pointed out that such devices have no structural function and are exclusively devoted to personal and/or equipment protection. They therefore do not require safety factor against yield limit, when operated in their highest performance regime. However, some safety margin is actually kept: the plastic zone between $\sigma_{0.2}$ and σ_R is wide enough to allow some creep in iron alloy without damage, and all dynamic calculations are performed assuming room temperature, so that elastic modulus and sound velocity of aluminium and copper alloys are slightly overestimated, as therefore are the stresses.

It should be emphasised that the analytical methods set out in this thermo-mechanical study are of general application, and may help in many other axi-symmetrical beam deposition analyses.

5.5 Maximum beam intensity

From an operational point of view, the results of this study are fully summarised in Table 17 and Fig. 28, which display the maximum allowed intensity of a $450\,GeV$ beam of radial size $\sigma_r = 0.58\,mm$, dumped every $16.8\,s$ on the TED and as single shot on the TBSE.

This intensity is given as a function of the pulse duration, from $0.1\,\mu s$ to $1.5\,s$. It is obtained by keeping constant the maximum equivalent stress σ_{teq} in copper, which is the most critical material: about $240\,MPa$ for slow pulses and $525\,MPa$ for pulses $\leq 6\,\mu s$. On the central part of the curve, from $10\,\mu s$ to $10\,ms$, the maximum allowed intensity is constant ($5\,10^{13}$ protons per pulse) as internal heat transfer has no time to develop while the pulse occurs, and the maximum temperature reached in the matter is therefore very close to the adiabatic one ΔT_0. On the right side of the curve, heat transfer becomes more and more effective during beam dumping, and the maximum reached temperature becomes smaller and smaller compared to the adiabatic one; mechanical limitations are therefore progressively replaced by thermal limitations. As already mentioned, $7\,10^{13}$ protons per pulse are greatly above the present possibilities of the PS-SPS complex. On the left side of the curve, the maximum allowed intensity rapidly decreases with the pulse duration t_0, as the dynamic radial stresses dominate more and more (the axial ones are independent of t_0 for such long cylinders) [13]. It therefore results that any beam intensity $\leq 4.2\,10^{13}$ protons per pulse may be dumped, under nominal beam parameters conditions, without pulse duration limitation.

Several remarks may help to extrapolate these results to beam parameters (energy, size, dumping repetition period) close to the nominal ones :

- increasing beam energy decreases the maximum allowed intensity, but less than proportionally as the ionisation process is independent of the incident proton energy,
- increasing beam section hitting the dump increases the maximum allowed intensity, but less than proportionally as the subsequent particle cascade is independent of the incoming beam size,
- increasing dumping repetition period increases the maximum allowed intensity, but less than proportionally as the maximum steady state temperature T_{max} is not proportionally affected, nor the thermo-mechanical material properties.

In practice, the maximum allowed beam intensity stated in Fig. 28 can be applied with confidence in the range of $400\,GeV$ to $500\,GeV$ beam energy, $0.5\,mm$ to $0.65\,mm$ beam size, and $10\,s$ to $20\,s$ dumping repetition period. Beyond these limits, new computations would be necessary.

6. Technical design

- A side view of the TED is presented in Fig. 29. In spite of various space and transportation problems, big efforts were spent to make the new TED for LHC dumps compatible with the present SPS ones. This results in several advantages :

- equipment standardisation,
- saving of one complete LHC spare (two common spares for both SPS and LHC are acceptable, only one specific spare for LHC would be critical) i.e. about $250\,KCHF$,
- genuine $450\,GeV$ beam absorption optimisation of the TED for LHC, as shown in section 4.1, whatever the intensity or frequency of the beam aborts.

The cast iron (GG20) external shielding is therefore identical to the present SPS one: two $4300 \times 960 \times 480\,mm$ yokes, $9.5\,tons$ each, water cooled by four independent circuits $\varnothing 16\,mm$, with handling and positioning facilities. The polycrystalline graphite (type R7500 from SGL) is split into twenty cylinders $\varnothing 80\,mm$, $145\,mm$ long, thermally shrink fitted at about $200\,°C$ into five aluminium tubes (EN AW 6082-T6) $\varnothing 80/160\,mm$, $600\,mm$ long, nested together and with a downstream solid cylinder of same length and same alloy. The six elements are assembled by means of elastic pins, and by four press fitted [15] stainless steel tubes $\varnothing 14/16\,mm$, twin-linked to form two independent water cooling circuits. This $160\,kg$ assembly

is housed into a (CuOFE) copper tube made of four elements ∅160/310 mm, 900 mm or 940 mm long, and of a downstream solid cylinder, 790 mm long. The five elements are also assembled by elastic pins and press fitted tubes, and are also cooled by two independent water circuits. This assembly method avoids expensive electron beam welding of special (and fairly brittle) copper alloy. A ∅58 mm insert, 250 mm long, made of special (UNS C17200) Cu-Be alloy, is shrink fitted by liquid nitrogen in the upstream part of the solid copper cylinder. The copper part of the dump core weighs about 2.4 tons and the complete TED weighs therefore about 21.6 tons. The eight independent water cooling circuits are fed by a collector located at the downstream end of the external shielding, which should provide a heat transfer coefficient $\geq 0.8 \, W/cm^2 \cdot °C$ to each circuit, with a maximum water speed of 2 m/s. In practice, a flow rate of about 18 m^3/h will be required for each TED.

- A side view of the TBSE is presented in Fig. 30. It is much simpler than the TED as it has neither external shielding nor cooling circuit. The inner graphite/aluminium core is made in the same way as the TED one, the aluminium elements being only assembled by elastic pins. The outer steel (C45 W) core is made of two pinned elements: a ∅120/240 mm tube, 3620 mm long, nesting a downstream solid cylinder, 500 mm long. The complete TBSE core weighs about 1.2 tons.

7. Conclusions

The optimised TED inner core consists of a ∅80 mm graphite cylinder 2.9 m long, housed into a ∅80/160 mm aluminium blind tube 3.5 m long, itself fitted into a ∅160/310 mm copper blind tube 4.3 m long. If embedded in the existing ∅960 mm outer iron shielding, it releases only 1.5 % of the beam energy, while embedded in a smaller ∅760 mm iron shielding the escaping energy would be 60 % higher, as well as the number of released neutrons. The design of the outer iron shielding of the existing SPS beam dumps will therefore be maintained.

The TBSE is made of the same graphite cylinder, housed into a ∅80/120 mm aluminium blind tube 3.5 m long, itself fitted into a ∅120/240 mm iron blind tube 4 m long. It releases 20 % of the beam energy.

Both TED and TBSE are designed to intercept up to $5 \, 10^{13}$ protons dumped in 6 µs, or $7 \, 10^{13}$ protons dumped in 1.5 s, the radial beam size being $\sigma_r = 0.58$ mm. Under such extreme conditions, the maximum temperatures would not exceed the acceptable values of 860 °C in graphite, 220 °C in aluminium, 260 °C in copper and 200 °C in iron. The most severe thermal stresses are located in the upstream copper part. The maximum allowed beam intensity for a safe operation is given as a function of the pulse duration, including slow pulses as presently aborted on SPS dumps. The analytical calculation methods set out in the thermo-mechanical part of this study are of general application, and may help in many other axi-symmetrical beam deposition analyses.

References

[1]   A. Hilaire, V. Mertens, E. Weisse, "Beam Transfer to and Injection into LHC", LHC Project Report 208 (1998).

[2]   The LHC Study Group, "The Large Hadron Collider – Conceptual Design", CERN/AC/95-05 (LHC), CERN Genève (20 October 1995).

[3]   "Parameters & Layout Committee", minutes of the 59th meeting – 12 April 2000.

[4]   A. Ijspeert, P. Sievers, "Proposal for a New External SPS Beam Dump", CERN/SPS/ABT/Int. 82-2 (1982).

[5]   E. Cennini et al., "SPS Safety Chain Modification for the LHC Transfer Lines and the Long Baseline Neutrino Facility", SL-Note 99-010 SLI (1999).

[6]   A. Fassò *et al*, in Proc. SARE-3, KEK-Tsukuba, ed H. Hirayama, KEK report Proceedings 97-5, (1997) 32; A. Fassò *et al*, "Electron-photon transport in FLUKA: status", and "FLUKA: Status and Perspectives for Hadronic Applications", in Proc. of MC2000 (Lisbon, Oct. 2000) (in press); http//www.cern.ch/fluka.

[7]   J.M. Zazula, G.R. Stevenson and E. Weisse, "Energy Deposition by SPS Beam in Targets of Various Materials", CERN SL/93-47 (BT) – November 1993.

[8]   G.W.C. Kaye and T.H. Laby, "Tables of Physical and Chemical Constants", Longman Scientific & Technical, New York (1971).

[9]   G.V. Samsonov, "Handbook of the Physicochemical Properties of elements", Plenum, New York (1968).

[10]   J. Avril, "Encyclopédie Vishay d'Analyse des Contraintes", Vishay-Micromesures, Malakoff, France - 1974.

[11]   H.S. Carslaw, J.C. Jaeger, "Conduction of Heat in Solids", Oxford University Press, 1992.

[12]   S. Timoshenko, "Résistance des Matériaux – Deuxième partie", Dunod, Paris - 1968.

[13]   S. Péraire, "Vibration d'un Cylindre Soumis à un Champ Thermique Radial", CERN SL/Note 97-39 BT/TA - May 1997.

[14]   M.R. Spiegel "Laplace Transforms" Schaum's Outline Series, McGraw-Hill, US 1965.

[15]   P. Gerdil, A. Ijspeert, "Cooling of absorber blocks by means of press fitted water tubes" CERN/SPS/ABT/Int. 82-3, Prévessin – October 1982.

Table 1 : Material properties at 20 °C.

	Density	Interaction length	Specific heat
Symbol	ρ		C_p
Unit	g/cm^3	cm	$J/g \cdot {}^oC$
Graphite	1.8	47.9	0.65
Aluminium	2.7	39.4	0.9
Copper	8.96	15.01	0.39
Tungsten	19.3	9.58	0.14
Iron	7.87	16.76	0.46
Cast Iron (96% Fe, 4%C)	7.64	16.9	

Table 2 : Escaping particles and their energy, for the optimised TED configuration.

	n	p	$\mu^\pm$	$\pi^\pm$	K	$e^\pm$	γ
Number/primary	598	0.96	0.11	0.95	0.25	1.3	96
Average energy (GeV)	0.0081	0.24	1.37	0.82	1.4	0.03	0.0034
Escaping energy (%)	72.1	3.3	2.2	11.5	5.3	0.6	4.9

Table 3 : Energy and particle containment balance, in the TED, per incident proton. The amounts of beam energy deposited as thermal energy (***Dep.***), employed to break the nuclear binding in endothermic nuclear reactions (***Bind.***), carried away by neutrinos *(ν E.)*, and carried by all other escaping particles (***Escaping***) are tabulated. The total neutron track length in the reference volume is also reported.

Configuration				(cm)	Leng.	Dep.	Bind.	ν E.	Escaping		n Track
C	Al	Cu	W		λ	%	GeV	GeV	GeV	%	cm
250	100	125		Old TED	16.4	91.6	26.6	5.1	6.0 ± 0.2	1.33	56000
250	100	80			13.1	91.5	26.3	5.1	6.7 ± 0.3	1.48	53900
250	100	80		76 cm Diam.	13.1	91.4	22.8	5	10.7 ± 0.5	2.38	86100
270	60	100			13.8	91.6	26.3	5.1	6.1 ± 0.2	1.36	52600
300	60	70			12.4	91.5	26.1	5	7.1 ± 0.3	1.58	53400
300	60	70		all Cu shell	12.4	91.6	26.1	4.9	6.6 ± 0.3	1.46	52900
300	60	50	20		13.2	91.3	27.9	5.1	6.2 ± 0.3	1.38	56000
300	50	80			12.8	91.6	26.2	5.1	6.9 ± 0.3	1.53	54000
290	60	80		Optimised	12.9	91.6	26.2	5.1	6.7 ± 0.3	1.49	53600

Table 4 : Peak energy density per incident proton and peak adiabatic temperature rise in the TED for $4.9\,10^{13}$ protons. Statistical errors are less than 10%.

Configuration				(cm)	Length	dE Al	dE Cu	ΔT Al	ΔT Cu
C	Al	Cu	W		λ	J/g	J/g	^{o}C	^{o}C
250	100	125		Old TED	16.4	$4.1\,10^{-12}$	$7.5\,10^{-13}$	210	95
250	100	80			13.1	$4.1\,10^{-12}$	$7.5\,10^{-13}$	210	95
270	60	100			13.8	$3.2\,10^{-12}$	$1.8\,10^{-12}$	170	220
300	60	70			12.4	$2.3\,10^{-12}$	$1.1\,10^{-12}$	120	135
300	60	50	20		13.2	$2.3\,10^{-12}$	$1.1\,10^{-12}$	120	135
300	50	80			12.8	$2.3\,10^{-12}$	$1.6\,10^{-12}$	120	200
290	60	80		Optimised	12.9	$2.4\,10^{-12}$	$1.2\,10^{-12}$	130	155
300	0	130			14.9		$6.1\,10^{-12}$		710
350	0	80			12.6		$2.1\,10^{-12}$		260

Table 5 : Energy containment, peak energy deposition per incident proton and peak temperature rise for $4.9\,10^{13}$ protons, in various TBSE configurations.

Configuration	Length	R Equiv.	Escaping En.		dE Fe	Δ T Fe
Unit	λ	λ	GeV	%	J/g	^{o}C
Old TBSE	23.9	0.61	76	17	$2.7\,10^{-10}$	>fusion
New, ∅160 mm Al	10.5	0.46	108	24	$1.3\,10^{-12}$	130
Optimised, ∅120 mm Al	10.5	0.54	89	20	$1.3\,10^{-12}$	130

Table 6 : Radial distribution model of energy density (d) and instantaneous temperature rise (ΔT) for $7\,10^{13}$ protons : $d(r) = d_0 \cdot \exp(-b_d \cdot r^2)$ and $\Delta T(r) = \Delta T_0 \cdot \exp(-b_T \cdot r^2)$.

Symbol	d_0	B_d	ΔT_0	b_T
Unit	J/cm^3	cm^{-2}	^{o}C	cm^{-2}
Graphite	3150	18.74	1140	15.44
Aluminium	460	0.18	180	0.17
Copper	784	0.19	220	0.19
Iron	744	0.21	190	0.2

Table 7 : Material properties at 20 °C (*continued from Table 1*).

	Thermal conductivity	*Thermal diffusivity*	*Thermal expansion*	*Elastic modulus*	*Poisson's ratio*	*Sound velocity*
Symbol	λ	a	α	E	ν	c
Unit	$W/cm \cdot °C$	cm^2/s	$\mu m/m \cdot °C$	GPa	-	$mm/\mu s$
Graphite	0.9	0.75	3	10	0.15	2.32
Aluminium	1.8	0.74	24	71	0.34	5.13
Copper	3.95	1.14	16.4	123	0.35	3.7
Iron	0.8	0.22	12.2	210	0.29	5.1

Table 8 : Typical figures for thermal transients due to 450 GeV fast and slow single pulses : radius R, cooling factor h, on-axis maximum temperature rise ΔT_{max}, time for ΔT_{max} to decrease by 1 % t_ε , time to reach ΔT_{max} for slow pulse t_{max}, time for external cooling to become effective t_c, time to reach a quasi-uniform exponential cooling t_u.

			Fast pulse ($5\ 10^{13}$ *protons in 6 μs*)				*Slow pulse* ($7\ 10^{13}$ *protons in 1.5 s*)			
Symbol	R	h	ΔT_{max}	t_ε	t_c	t_u	ΔT_{max}	t_{max}	t_c	t_u
Unit	cm	cm^{-1}	$°C$	ms	s	s	$°C$	s	s	s
Graphite	4	0.44	840	1.5	0.8	2.1	190	0.9	1.2	8.5
Aluminium	8	0.16	130	20	0.7	80	145	1.1	1.1	90
Copper	15.5	0.04	160	12	6.6	50	160	1.05	6.7	60
Iron	12	0.005	140	80	17	150	175	1.15	16.4	160

Table 9 : Typical figures for periodic cycling due to repeated 450 GeV fast and slow pulses : time constant of exponential cooling τ, on-axis extreme steady state temperatures T_{max} and T_{min}, number of cycles and related time for steady state to set up N_s and $N_s \cdot t_p$ ($t_p = 16.8$ s).

		Fast pulse ($5\ 10^{13}$ *protons in 6 μs*)				*Slow pulse* ($7\ 10^{13}$ *protons in 1.5 s*)			
Symbol	τ	T_{max}	T_{min}	N_s	$N_s \cdot t_p$	T_{max}	T_{min}	N_s	$N_s \cdot t_p$
Unit	s	$°C$	$°C$	-	s	$°C$	$°C$	-	s
Graphite	6.06	860	21	5	84	211	22	6	101
Aluminium	33.8	190	65	29	487	218	80	20	336
Copper	170	238	80	99	1663	257	103	71	1193

Table 10 : Boundary condition coefficients *m* and *n* as functions of radial and axial expansion freedom.

Radial expansion	Axial expansion	m	n	Index
free	free uniform	1	1	a
free	prevented	1	ν	b
prevented	free uniform	-1	1	c
prevented	prevented	$-\dfrac{1}{1-2\nu}$	$-\dfrac{\nu}{1-2\nu}$	d

Table 11 : Extreme amplitudes of quasi-static thermal stresses σ_r, σ_θ and σ_z, generated on-axis by a 1.5 s slow pulse of 7 10^{13} protons. Maximum equivalent Stassi stress σ_{teq} to be compared to the tensile strength limit σ_0 (= yield limit $\sigma_{0,2}$ for metallic material).

	Free radial expansion	Radial & Tangential stresses	Longitudinal stress	Equivalent Stassi stress	σ_0'/σ_0	Tensile strength limit
Symbol	-	$\sigma_{r\,extr} = \sigma_{\theta\,extr}$	$\sigma_{z\,extr}$	$\sigma_{teq\,max}$	k_s	σ_0
Unit	-	MPa	MPa	MPa	-	MPa
Graphite	no	-3.9	-7.5	0.4	3.3	>25
Aluminium	yes	-170	-340	170	1	200 (320)
Copper	yes	-240	-480	240	1	70 (550)
Iron	yes	-350	-700	350	1	150 (370)

Table 12 : Extreme amplitudes of mean dynamic stresses $\sigma_{r\,i}(r)$, $\sigma_{\theta\,i}(r)$ and $\sigma_{z\,i}(r)$ and of initial displacements $-u_i(r)$ and $-w_i(z)$, generated by a 6 µs fast pulse of 5 10^{13} protons.

			Stresses		Displacements	
Symbol	R	L	$\sigma_{r\,i}(0) = \sigma_{\theta\,i}(0)$	$\sigma_{z\,i}(0)$	$-u_{i\,max}$	$-w_i(L)$
Unit	cm	cm	MPa	MPa	µm	µm
Graphite	4	7.25	-24	-48	-1.7	-1.7
Aluminium	8	30	-159	-318	-31.3	-85.8
Copper	2.9	12.5	-188	-376	-20.7	-88.4
Iron	12	25	-273	-546	-12.4	-15.5

Table 13 : Minimum and maximum values of the principal dynamic stresses σ_r, σ_θ and σ_z generated on-axis by the radial shock wave (of pseudo-period t_r) induced by instantaneous and 6 µs pulses of 5 10[13] protons.

Symbol	t_r	Instantaneous pulse				6 µs pulse			
		$\sigma_{r\,=\,}\sigma_\theta$		σ_z		$\sigma_{r\,=\,}\sigma_\theta$		σ_z	
Unit	µs	MPa		MPa		MPa		MPa	
		min	max	min	max	min	max	min	max
Graphite	>54	−32	32	−10	10	−3	3	−1	1
Aluminium	38	−540	505	−335	320	−240	215	−130	120
Copper	19	−900	1380	−695	860	−405	410	−160	160
Iron	>64	−640	610	−360	345	−240	215	−125	115

Table 14 : Extreme amplitudes of the axial dynamic stresses $\sigma_{z\,extr}$ generated in the middle of the cylinder by the longitudinal shock wave (of period t_z) induced by instantaneous or 6 µs pulses of 5 10[13] protons.

Symbol	t_z	$\sigma_{z\,extr}$
Unit	µs	MPa
Graphite	125	±0.23
Aluminium	234	±20
Copper	135	±87
Iron	196	±13

Table 15 : Oscillation limits of the total principal stresses σ_r, σ_θ and σ_z and of the equivalent Stassi stress σ_{teq} generated at $r = 0$ and $z = 0$ by the mechanical shock wave induced by a 6 µs pulse of 5 10[13] protons.

	Free radial expansion	Radial & Tangential stresses		Longitudinal stress		Equivalent Stassi stress	
Symbol	-	$\sigma_{r\,=\,}\sigma_\theta$		σ_z		σ_{teq}	
Unit	-	MPa		MPa		MPa	
		min	max	min	max	min	max
Graphite	no	−27	−21	−49	−47	2	3.2
Aluminium	yes	−395	53	−435	−180	30	275
Copper	yes	−595	220	−620	−140	0	525
Iron	yes	−510	−60	−660	−425	145	385

Table 16 : Minimum yield limit $\sigma_{0,2}$, alternating fatigue limit σ_f and ultimate strength σ_R, assumed for aluminium, copper and iron alloys.

	Name	*Chemical composition*	*Yield limit*	*Alternating fatigue limit*	*Ultimate strength*
Symbol	-	**-**	$\sigma_{0,2}$	σ_f	σ_R
Unit	-	*%*	*MPa*	*MPa*	*MPa*
Aluminium alloy	EN AW 6082	1 Si, 0.9 Mg, 0.7 Mn	320	±170	350
Copper alloy	UNS C17200	1.9 Be, 0.2 Co	550	±320	650
Iron alloy	C45 W	0.45 C	370	-	540

Table 17 : Maximum allowed intensity I_{max} of a 450 GeV beam of radial size 0.58 mm dumped every 16.8 s, as a function of the pulse duration t_0.

Pulse duration	*Maximum Intensity*
t_0	I_{max}
μs	$10^{13}\ p$
0.1	4.25
1	4.3
2	4.38
3	4.5
4	4.7
5	4.95
6	5
10^3	5
10^4	5
$5\ 10^4$	5.02
10^5	5.1
$2\ 10^5$	5.25
$3\ 10^5$	5.4
$5\ 10^5$	5.7
10^6	6.4
$1.5\ 10^6$	7
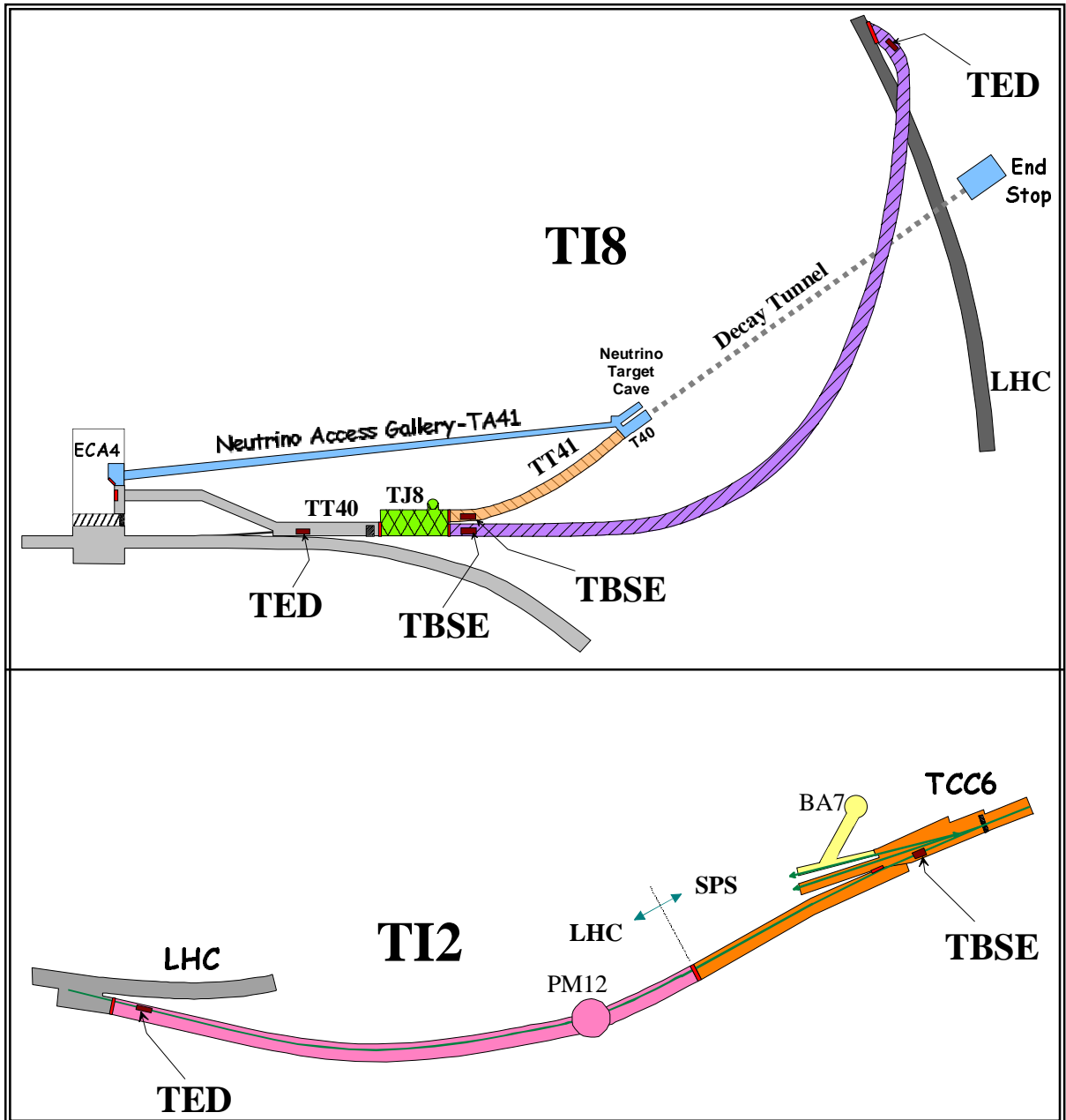
Figure 1 : Schematic views of the LHC and CNGS transfer lines, showing TED and TBSE location.

OLD TED

NEW TED

a)

OLD TBSE

NEW TBSE

b)
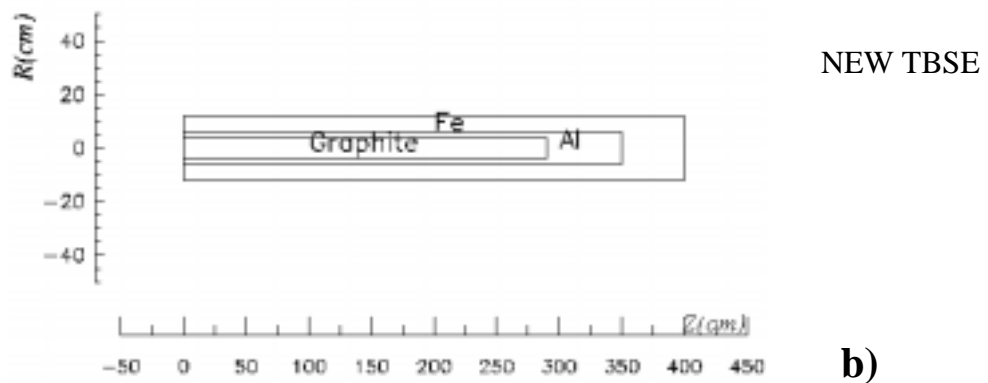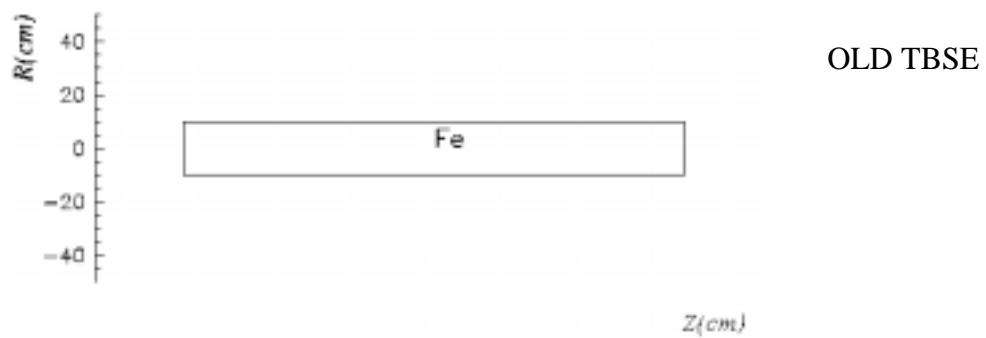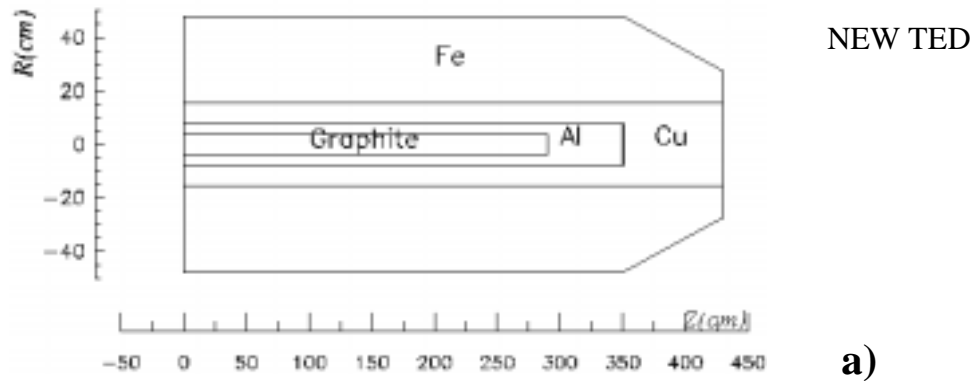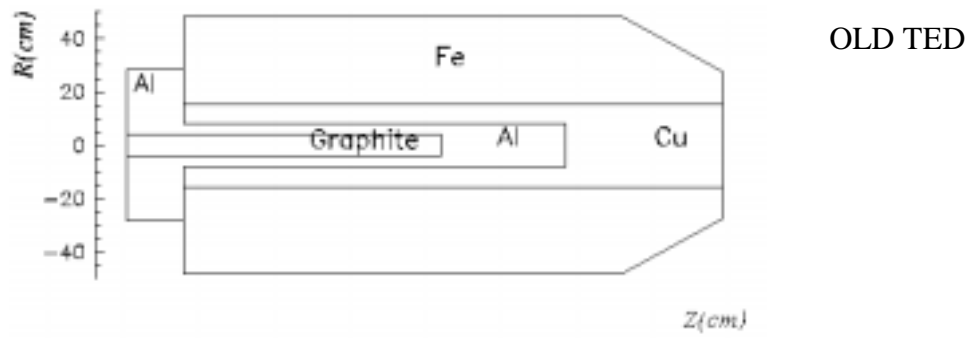
Figure 2 : a) Layout of the old (top) and new (bottom) TED beam dump; **b)** Layout of the old (top) and new (bottom) TBSE.

31
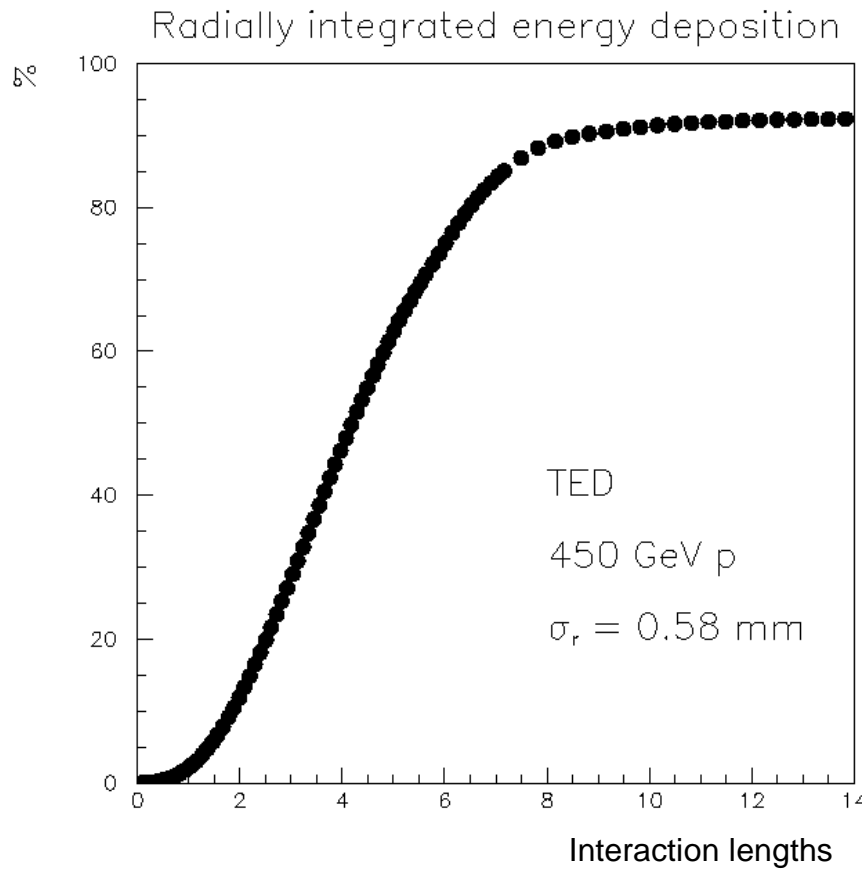
Figure 3 : Radially integrated energy deposition in the TDE, as a function of its length, normalised to the beam energy.
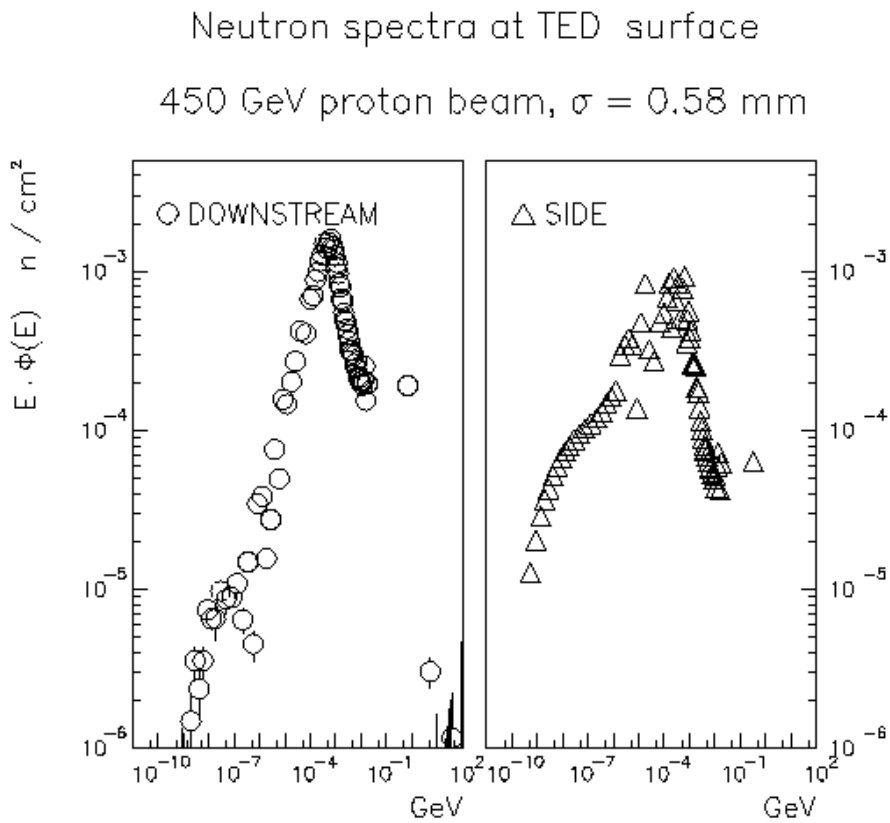
Figure 4 : Energy-weighted neutron spectra at the TED surfaces.

450 GeV protons, $\sigma = 0.58$ mm

OLD TED

OUTER IRON SHIELDING $\varnothing$ 760 mm

OPTIMISED TED

NEUTRON FLUENCE (n / cm^2· proton)
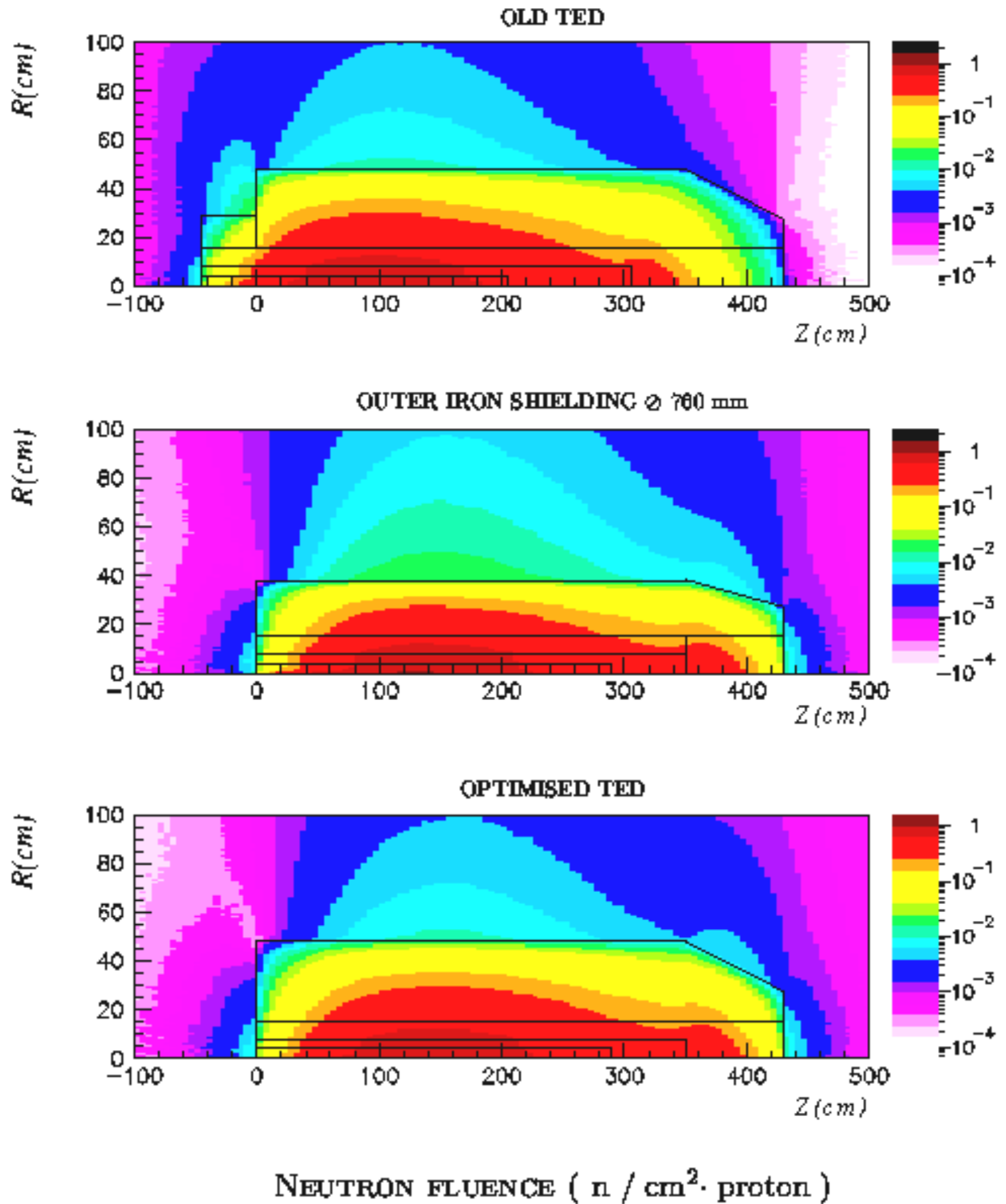
Figure 5 : Neutron fluence in and around the TED for the old (top), smaller (middle) and new (bottom) configurations, normalised to one incoming proton.
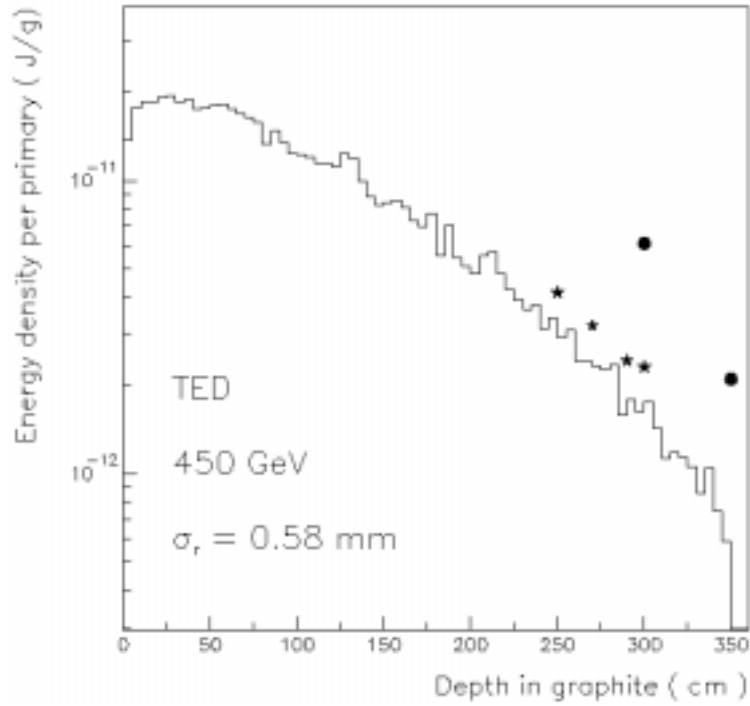
Figure 6 : Energy density around the beam axis as a function of depth, for an homogeneous graphite absorber (histogram). Maximum energy density in aluminium (stars) or copper (dots) layers placed after selected graphite lengths.
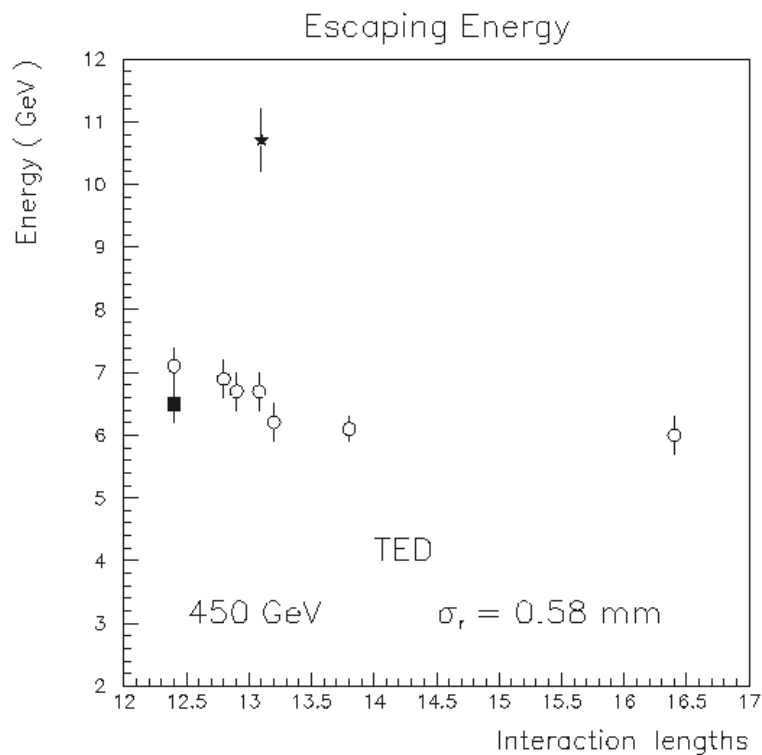
Figure 7 : Energy escaping from the TED, as a function of its length, for a 450 GeV proton beam. Results are normalised to one incident proton. Open dots: existing iron shield ⌀960 mm. Black star: shield ⌀760 mm. Black square: substitution of the outer aluminium shell with a copper shell.

34

Longitudinal shower development

TED

450 GeV

$\sigma_r = 0.58$ mm
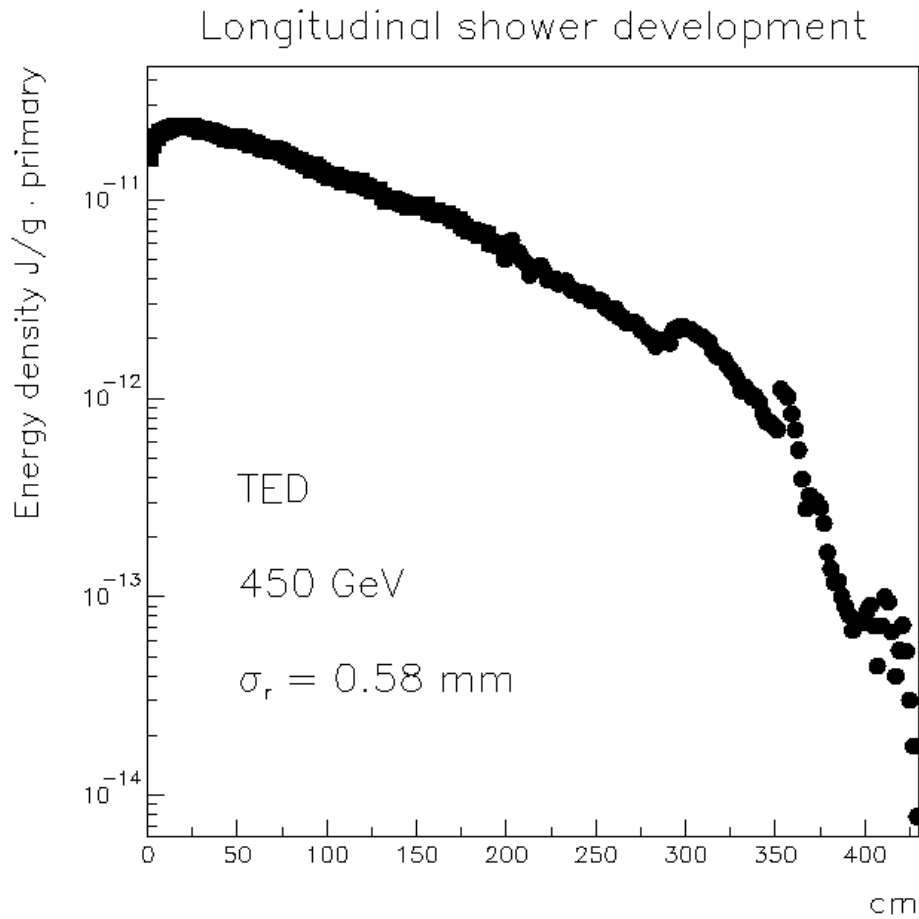
Figure 8 : Energy density along the beam axis in the optimised TED, normalised to one incoming proton. Energy is scored within a radius of 0.25 mm up to 200 cm, and within 1 mm afterwards.

Radial profile

● Al   ■ Cu

TED   450 GeV

$\sigma_r = 0.58$ mm
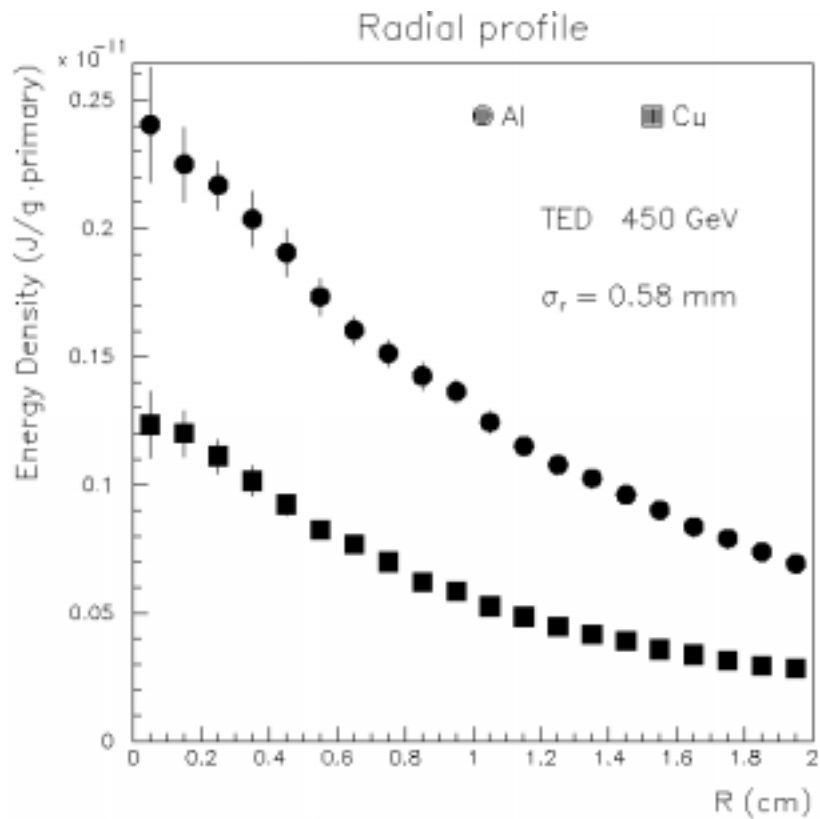
Figure 9 : Energy density as a function of radius in the optimised TED core, at the depths corresponding to the peak depositions in aluminium and copper.
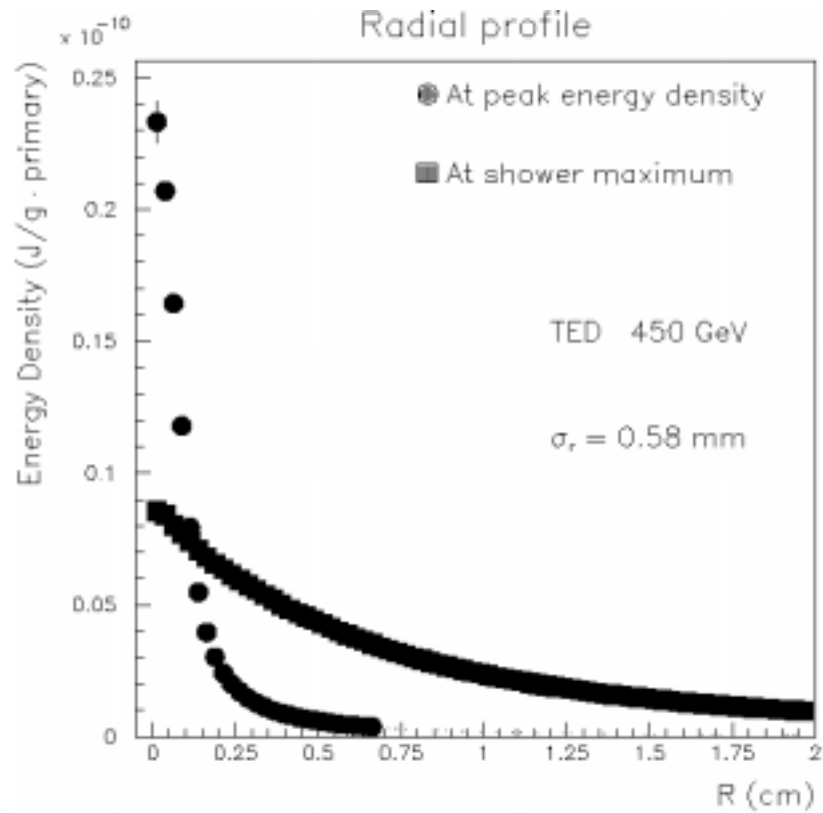
Figure 10 : Energy density as a function of radius in the optimised TED core, at the depths corresponding to the peak energy density in graphite (dots) and to the maximum of the radially integrated energy deposition (squares).
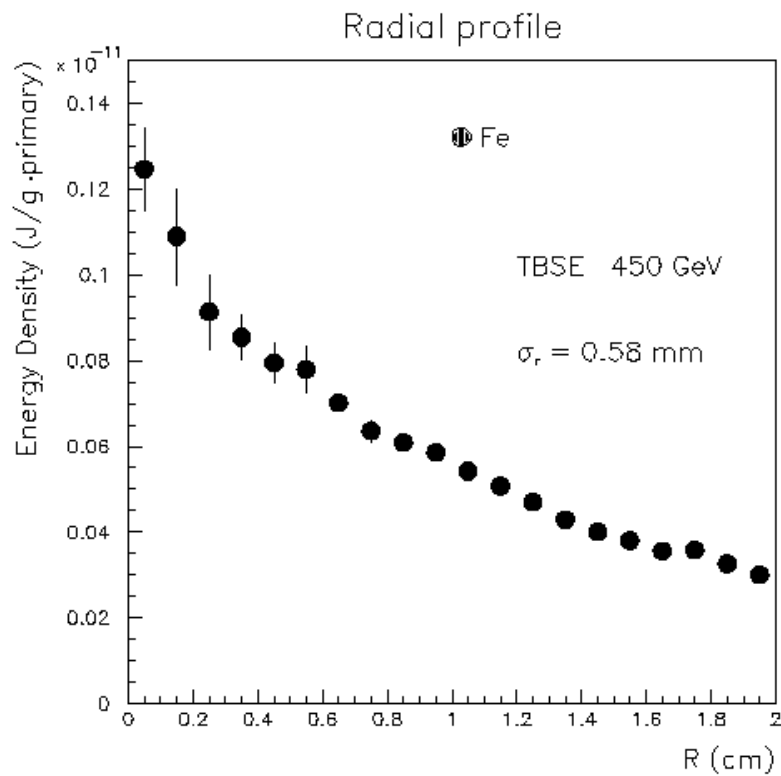
Figure 11 : Energy density as a function of radius in the optimised TBSE core, at the depths corresponding to the peak depositions in iron.
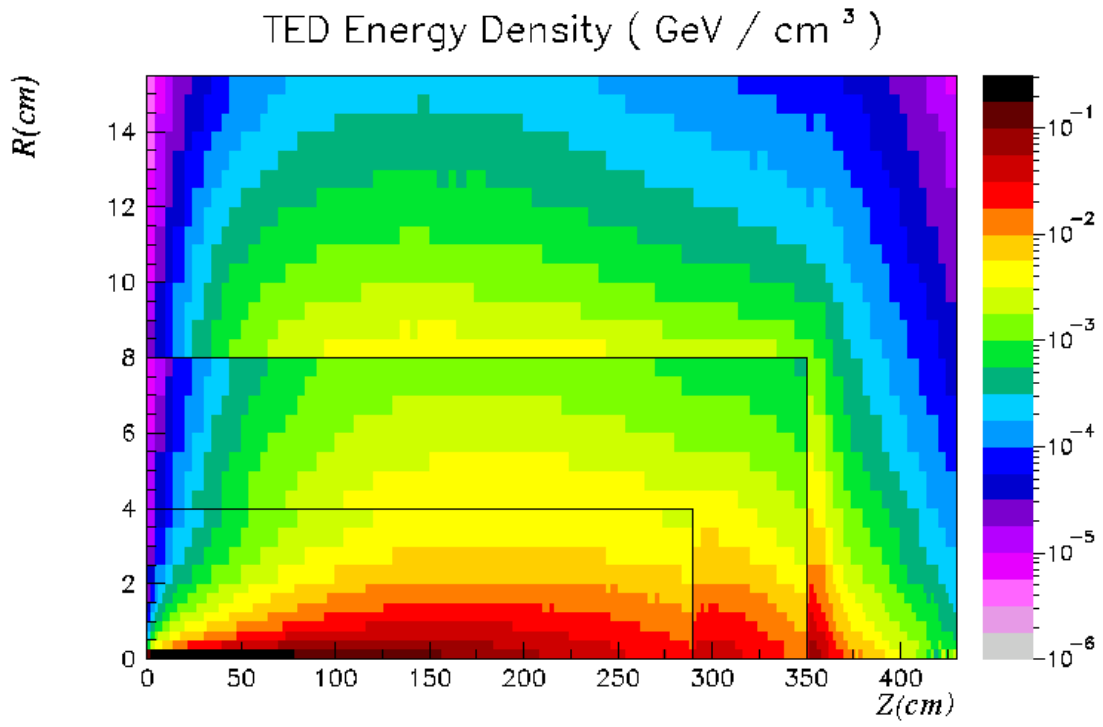
Figure 12 : Map of the deposited energy density in the optimised TED core. Normalised to one incident proton at 450 GeV.
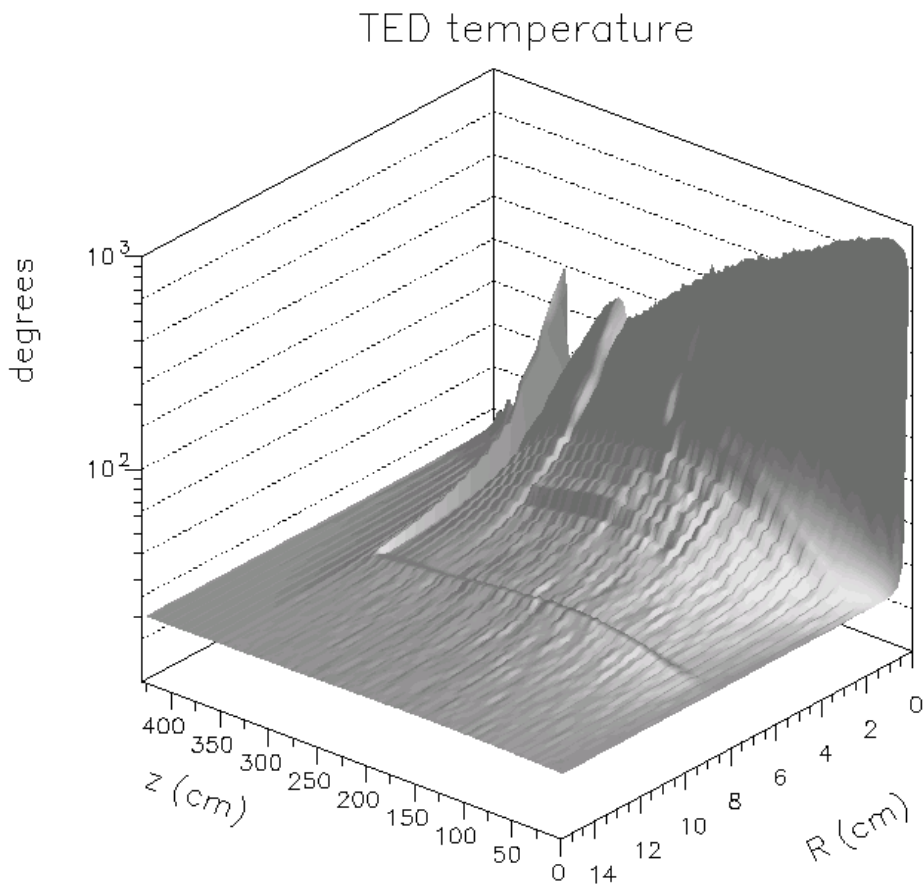
Figure 13 : Instantaneous temperature (°C) reached in the TED core when hit by an ultimate intensity batch of 4.9 10^{13} protons at 450 GeV.
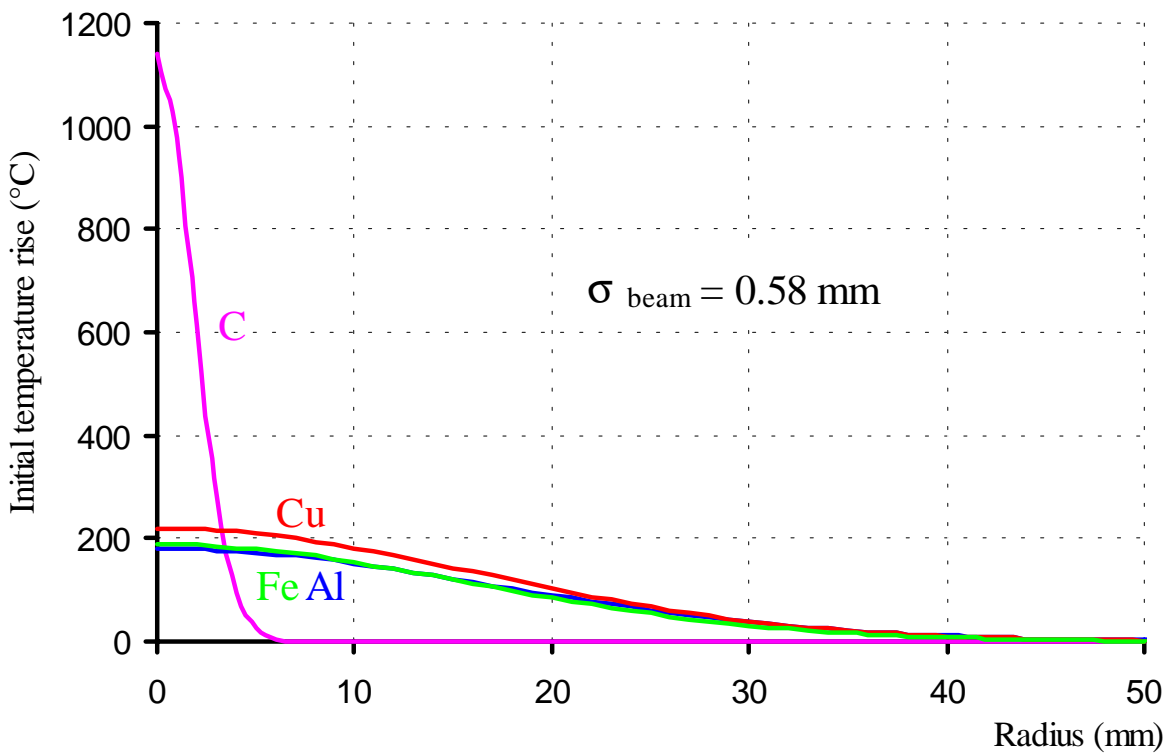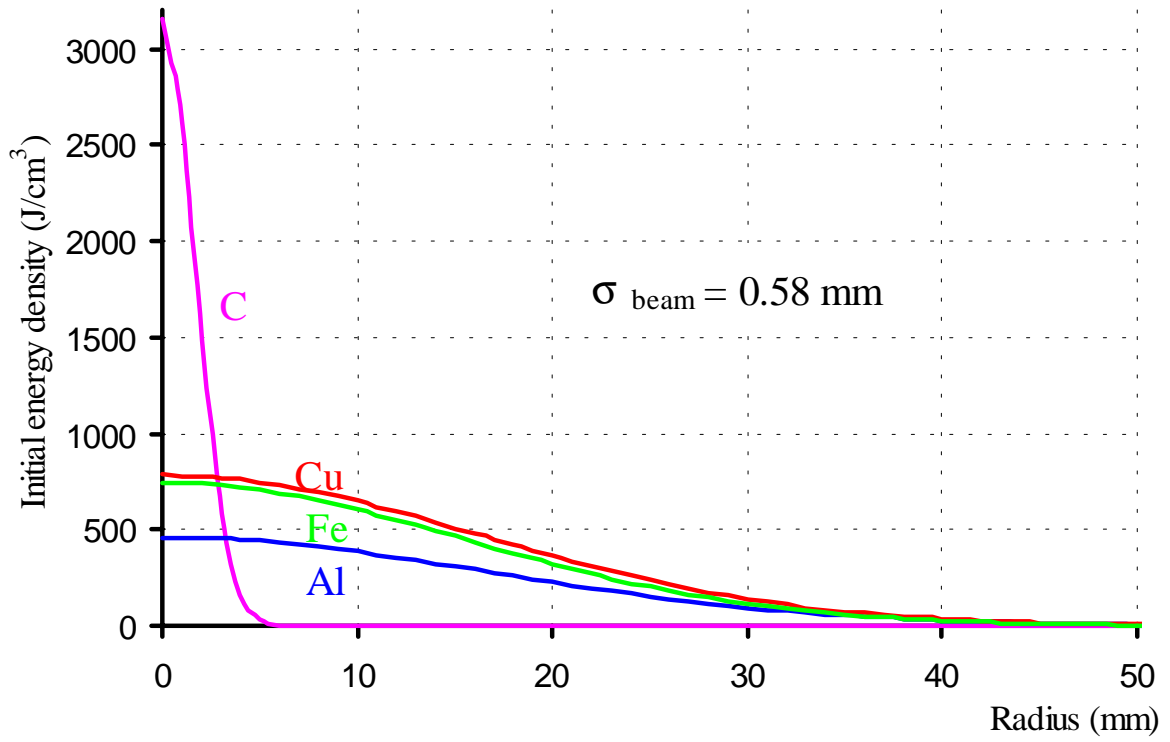
Figure 14 : Radial distribution of initial energy density and temperature rise induced by 7 10^{13} protons at 450 GeV.
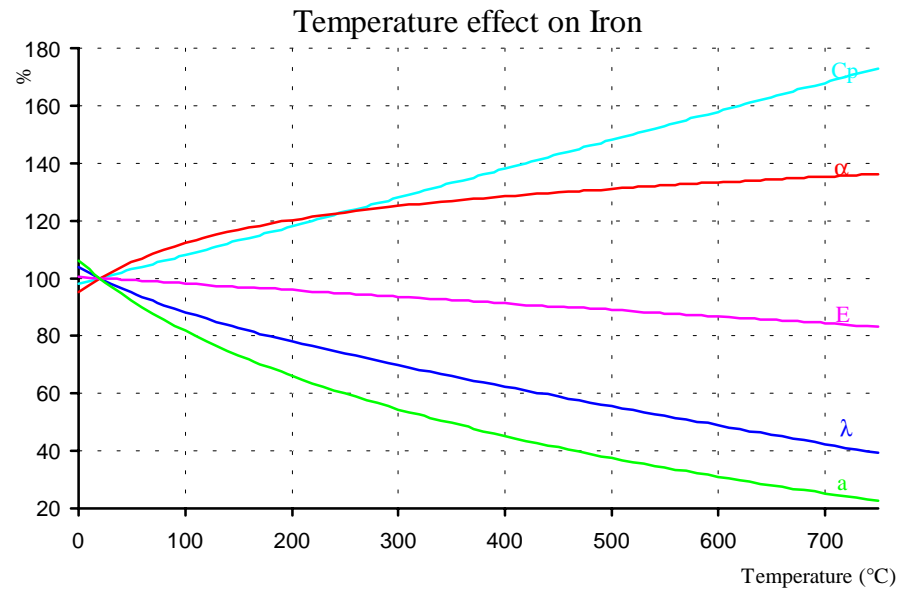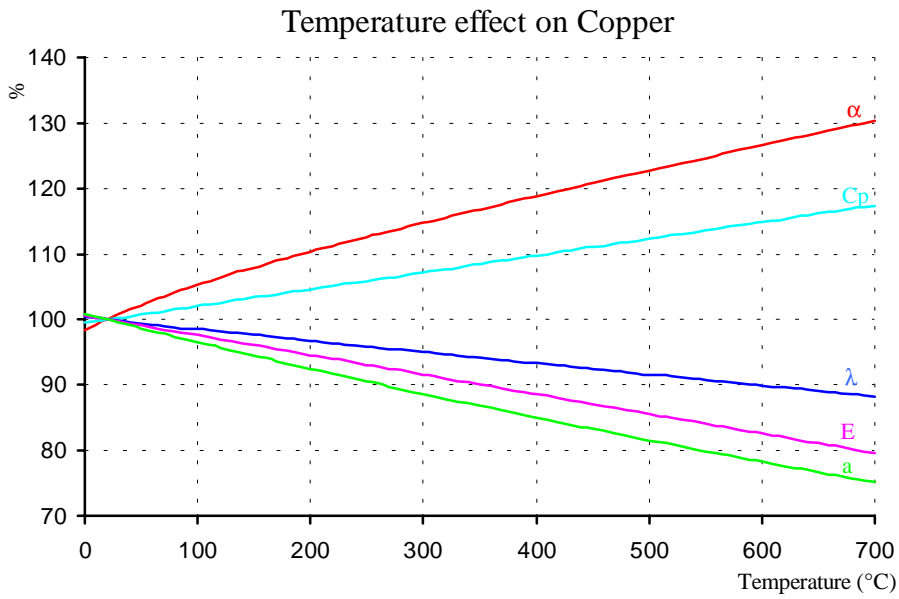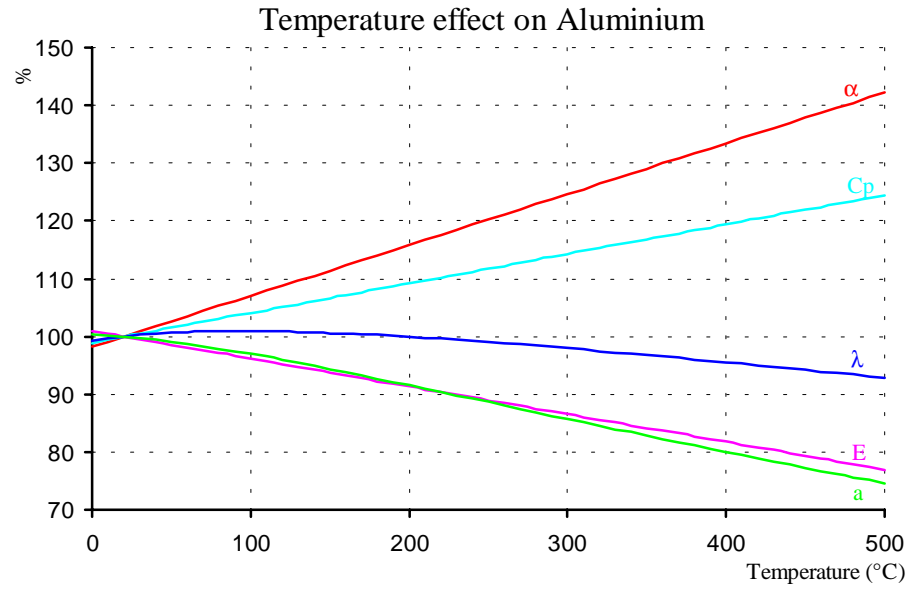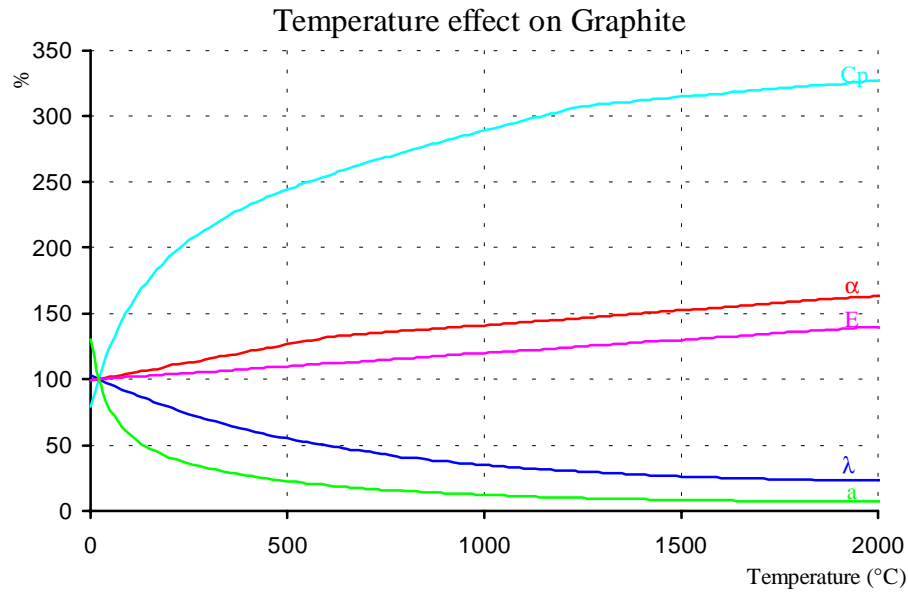
Figure 15 : Temperature evolution of thermal and mechanical properties, related to room temperature.
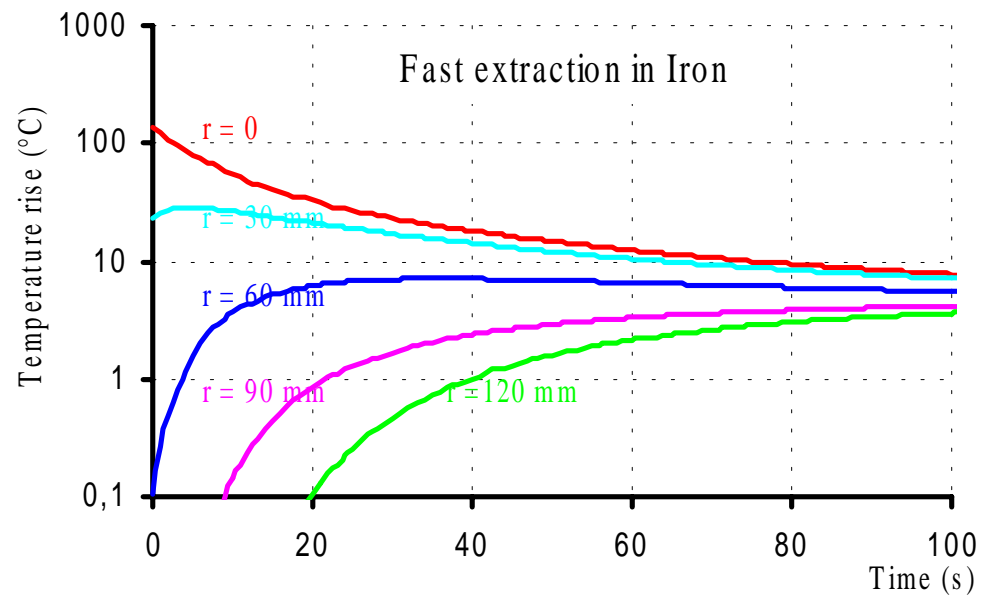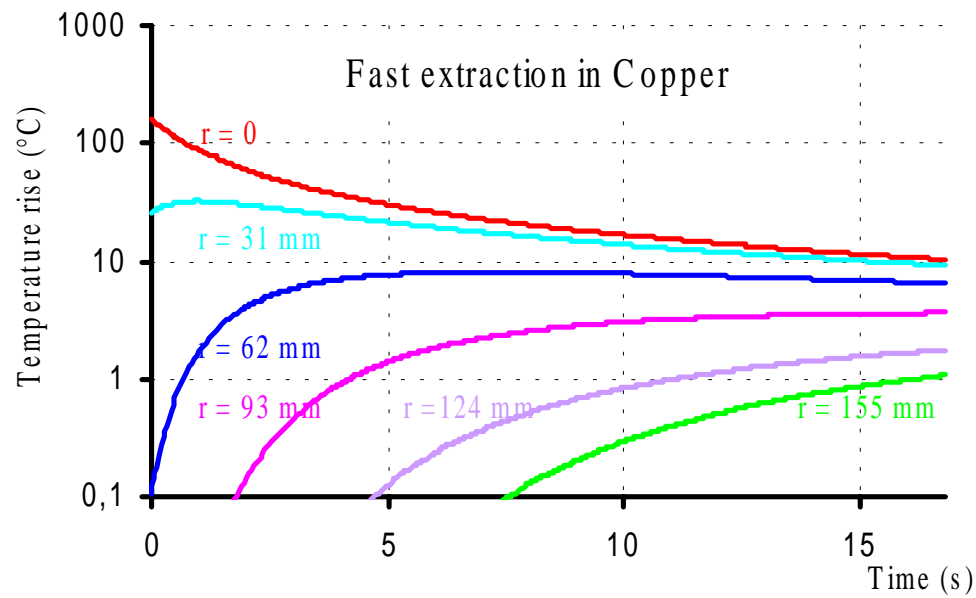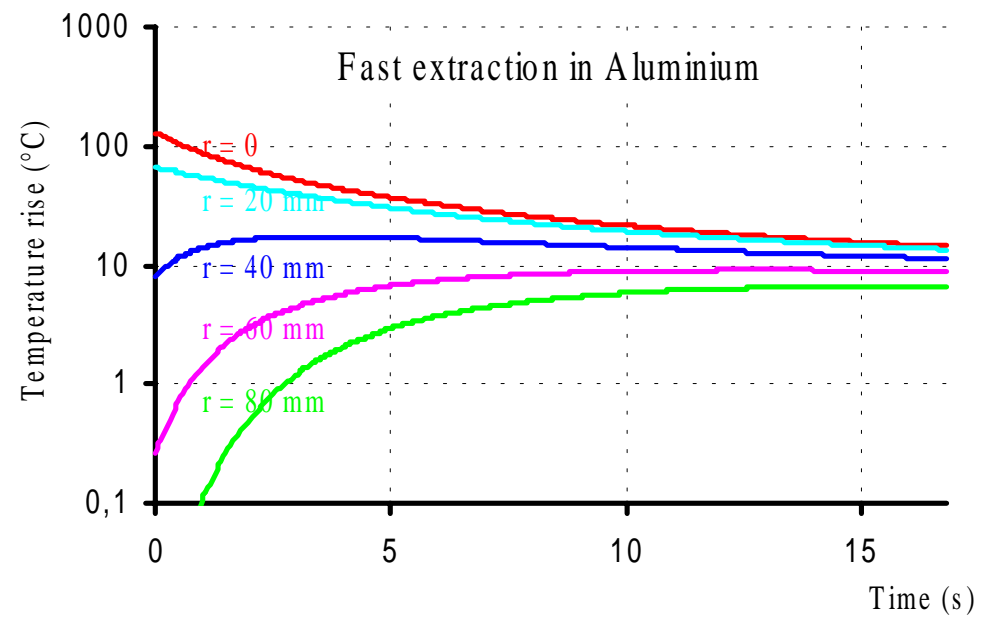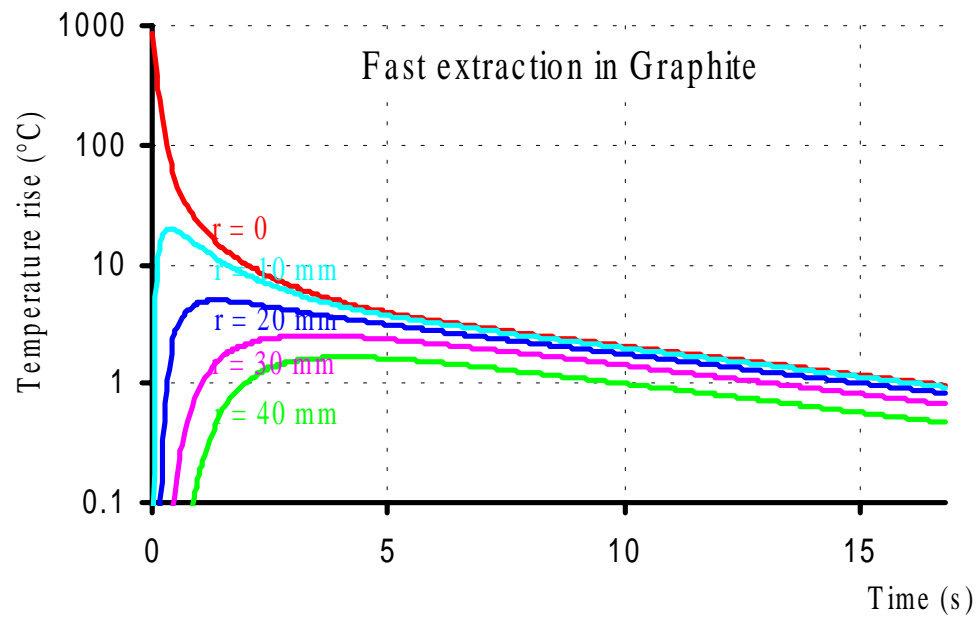
Figure 16 : Transient evolution of an instantaneous 450 GeV single pulse of 5 10^{13} protons.
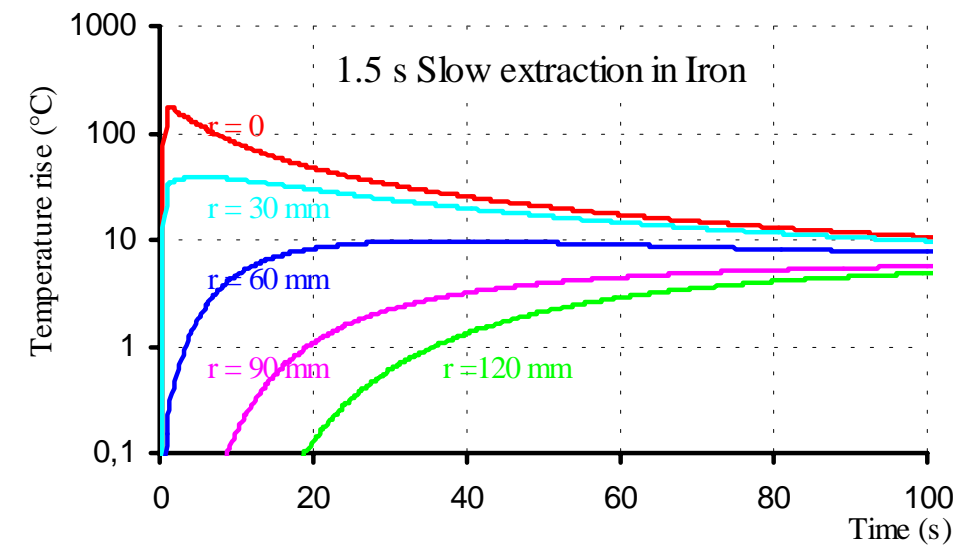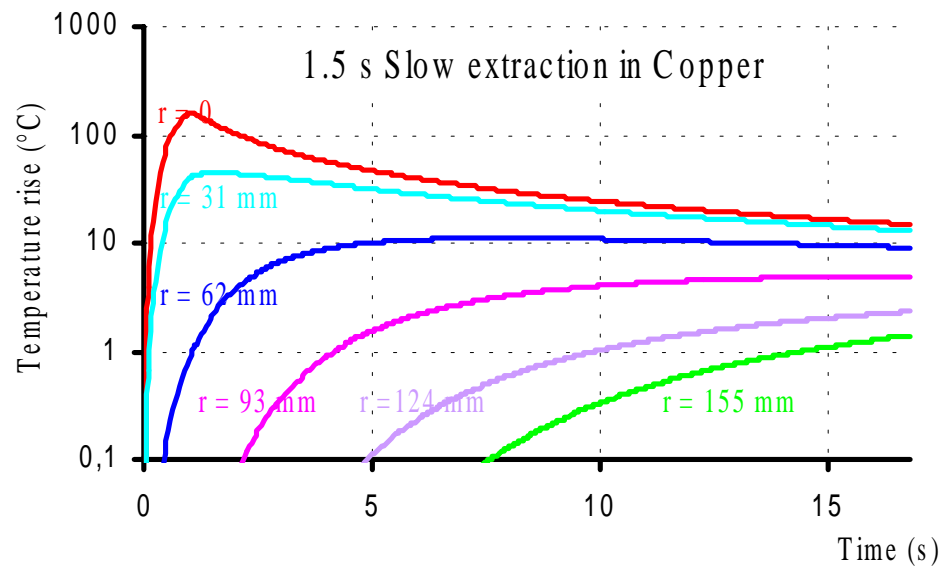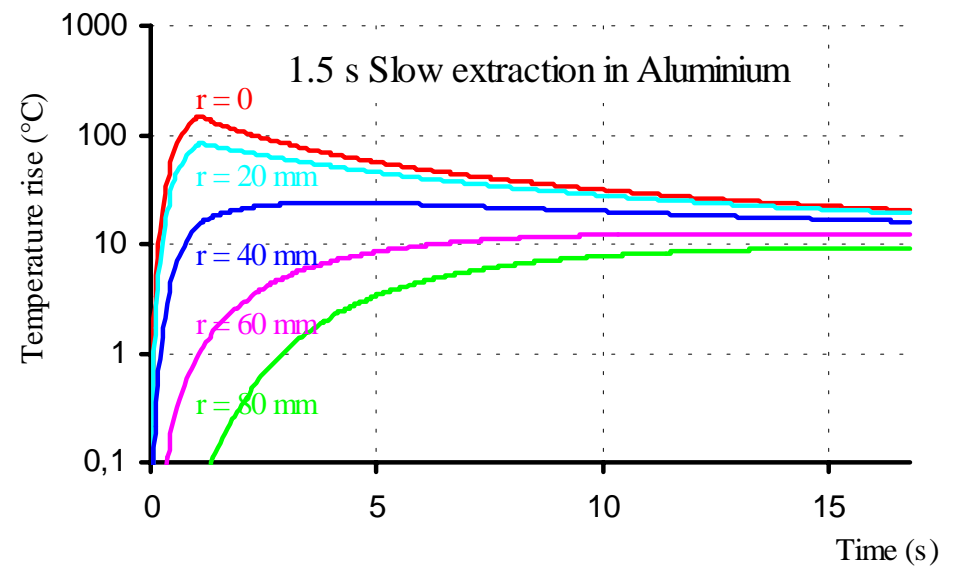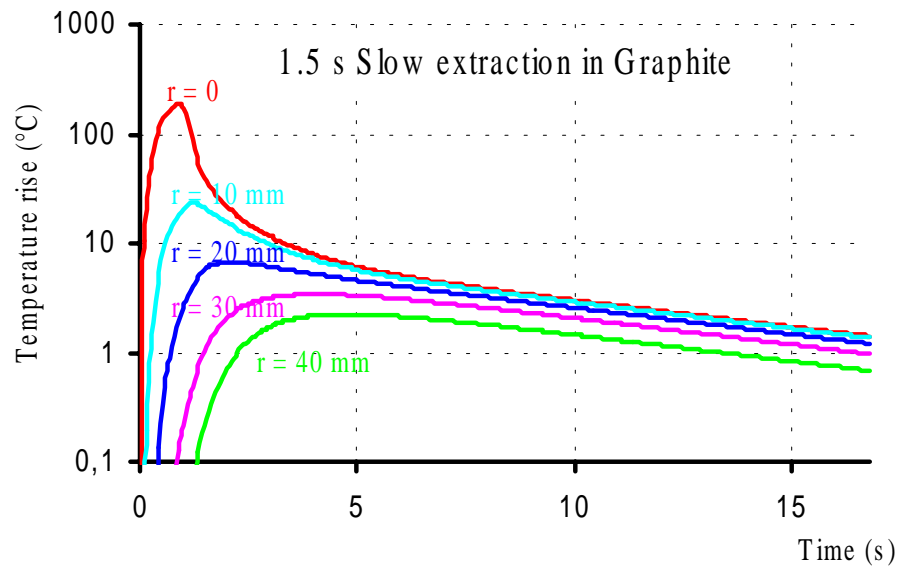
Figure 17 : Transient evolution of a slow 450 GeV single pulse of 7 10^{13} protons dumped in 1.5 s.
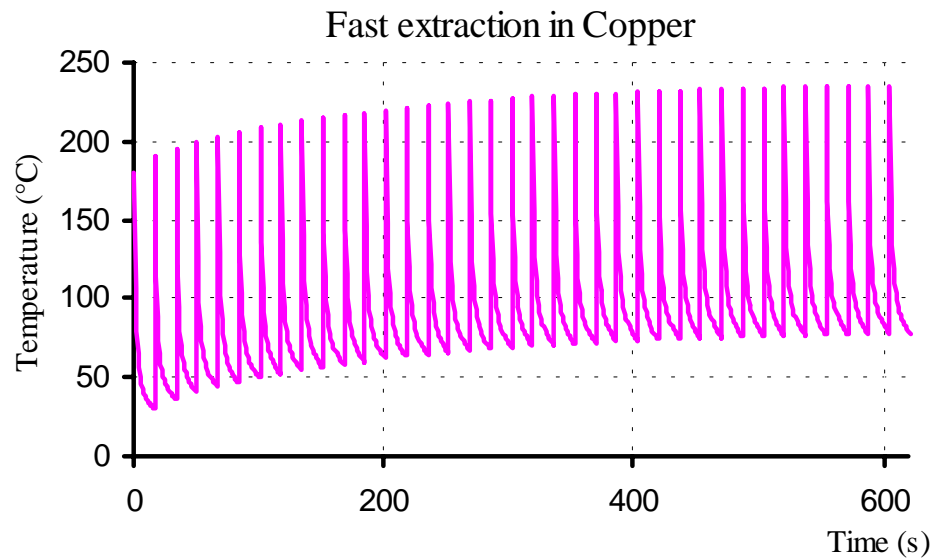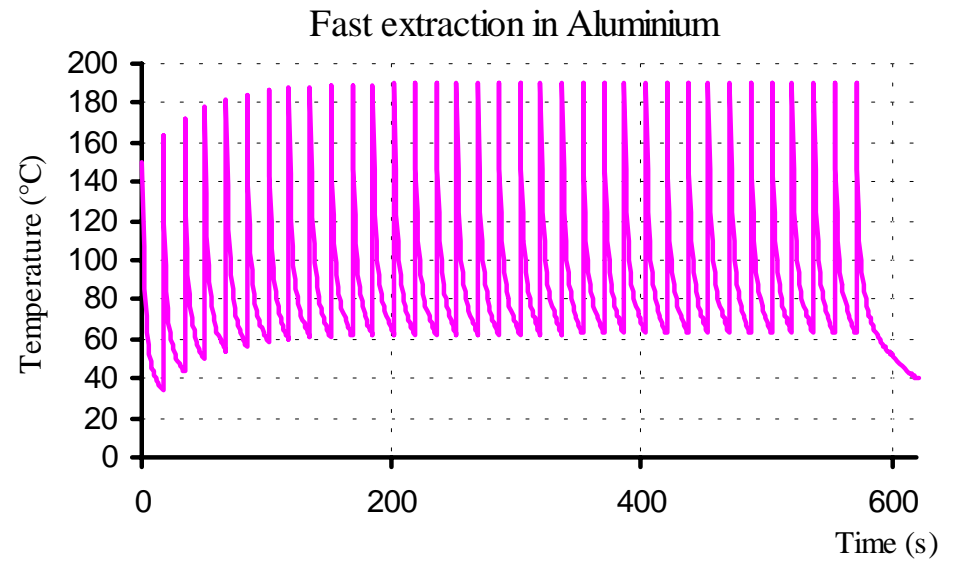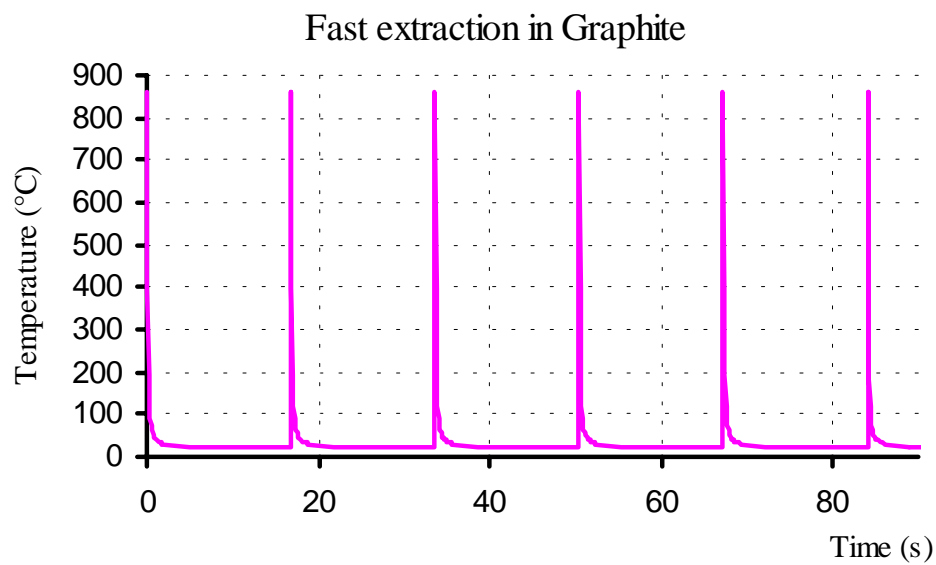
Figure 18 : Thermal cycling generated by successive 6 μs pulses dumped every 16.8 s.
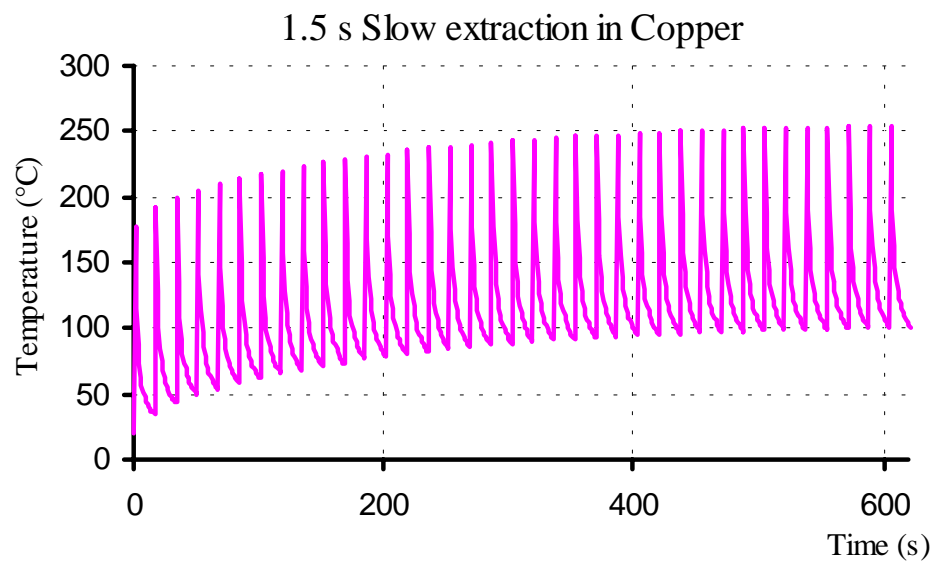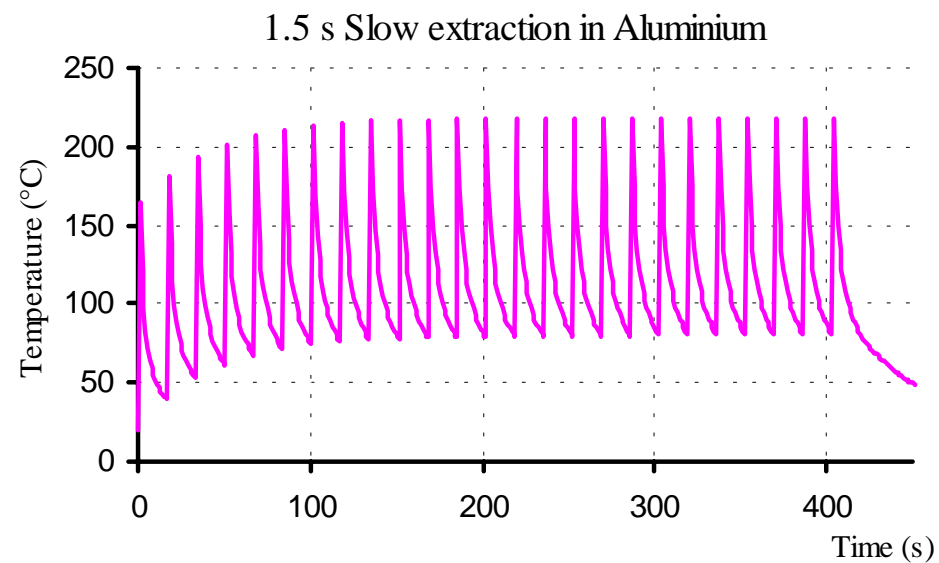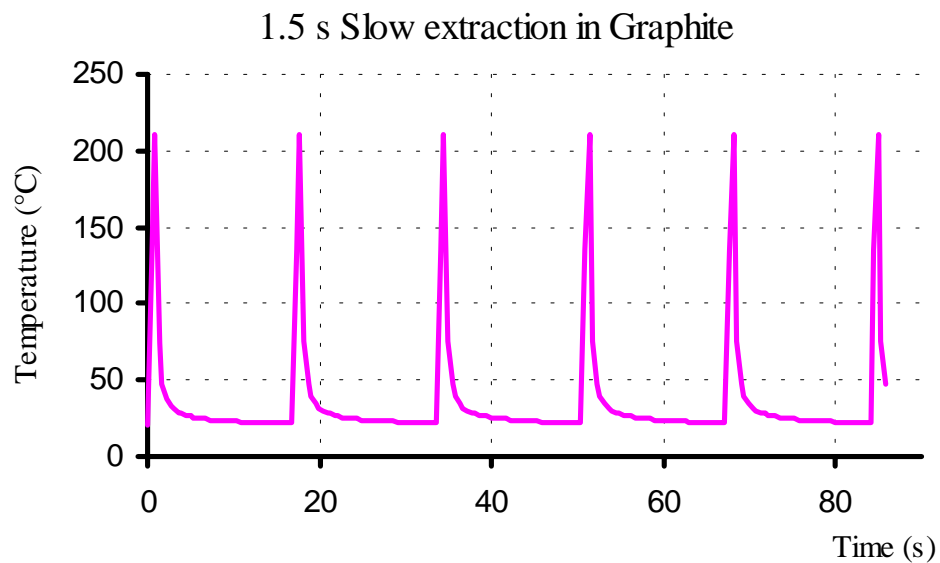
Figure 19 : Thermal cycling generated by successive 1.5 s pulses dumped every 16.8 s.

43
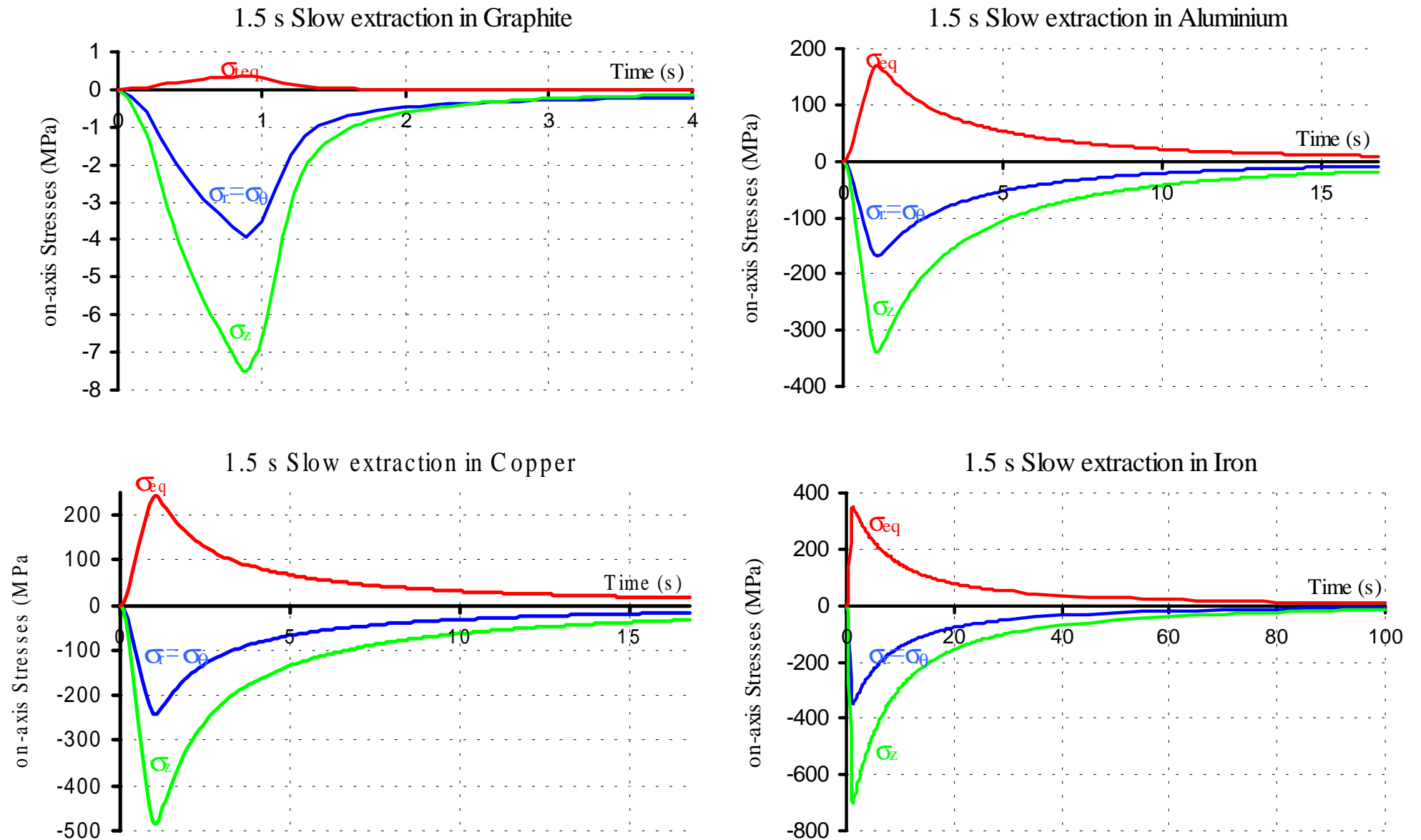
Figure 20 : Time evolution of the principal quasi-static thermal stresses generated on-axis by a 1.5 s pulse of 7 10^{13} protons.
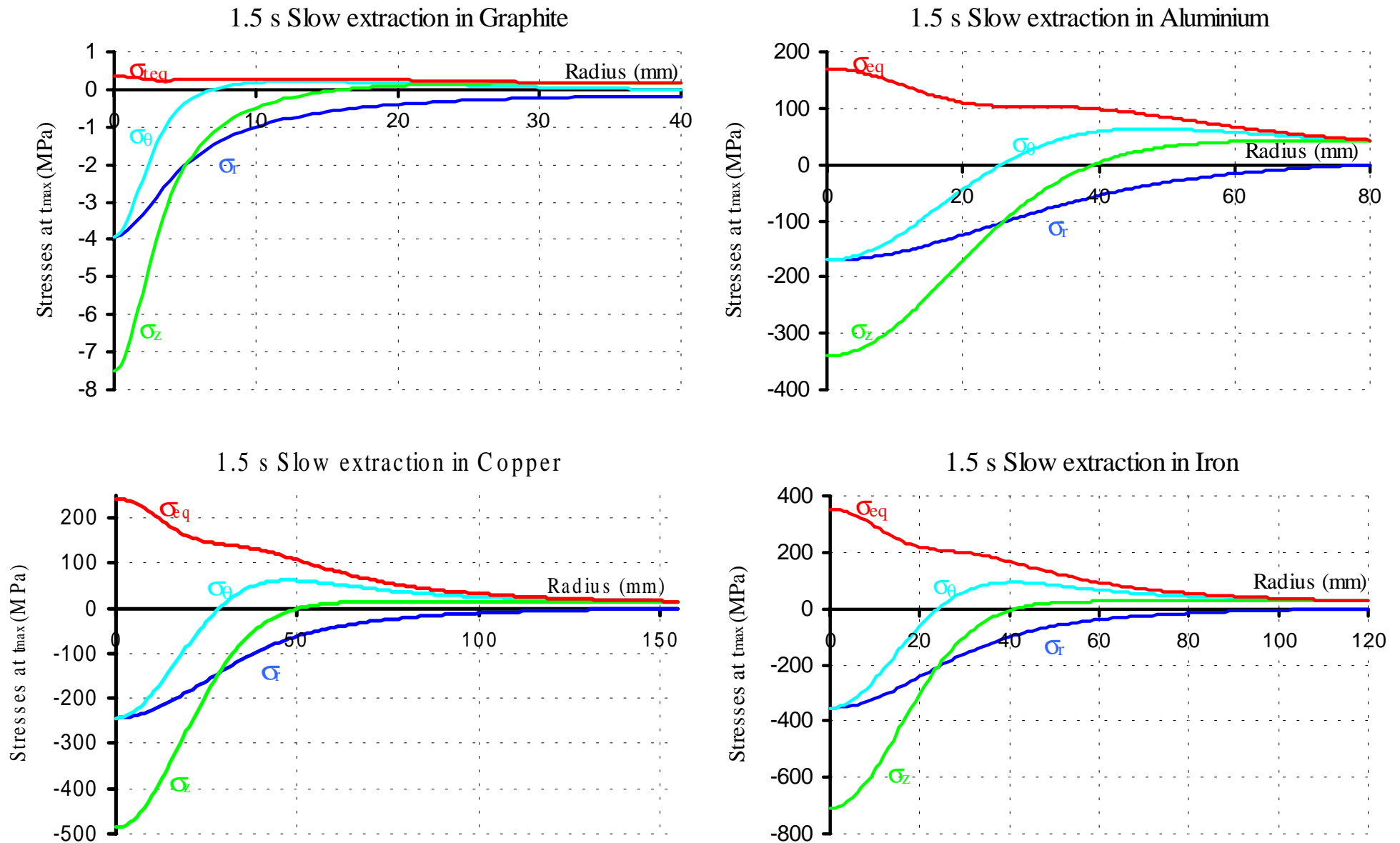
Figure 21 : Radial distribution of the principal quasi-static thermal stresses generated by a 1.5 pulse of 7 10^{13} protons at time t_{max}.
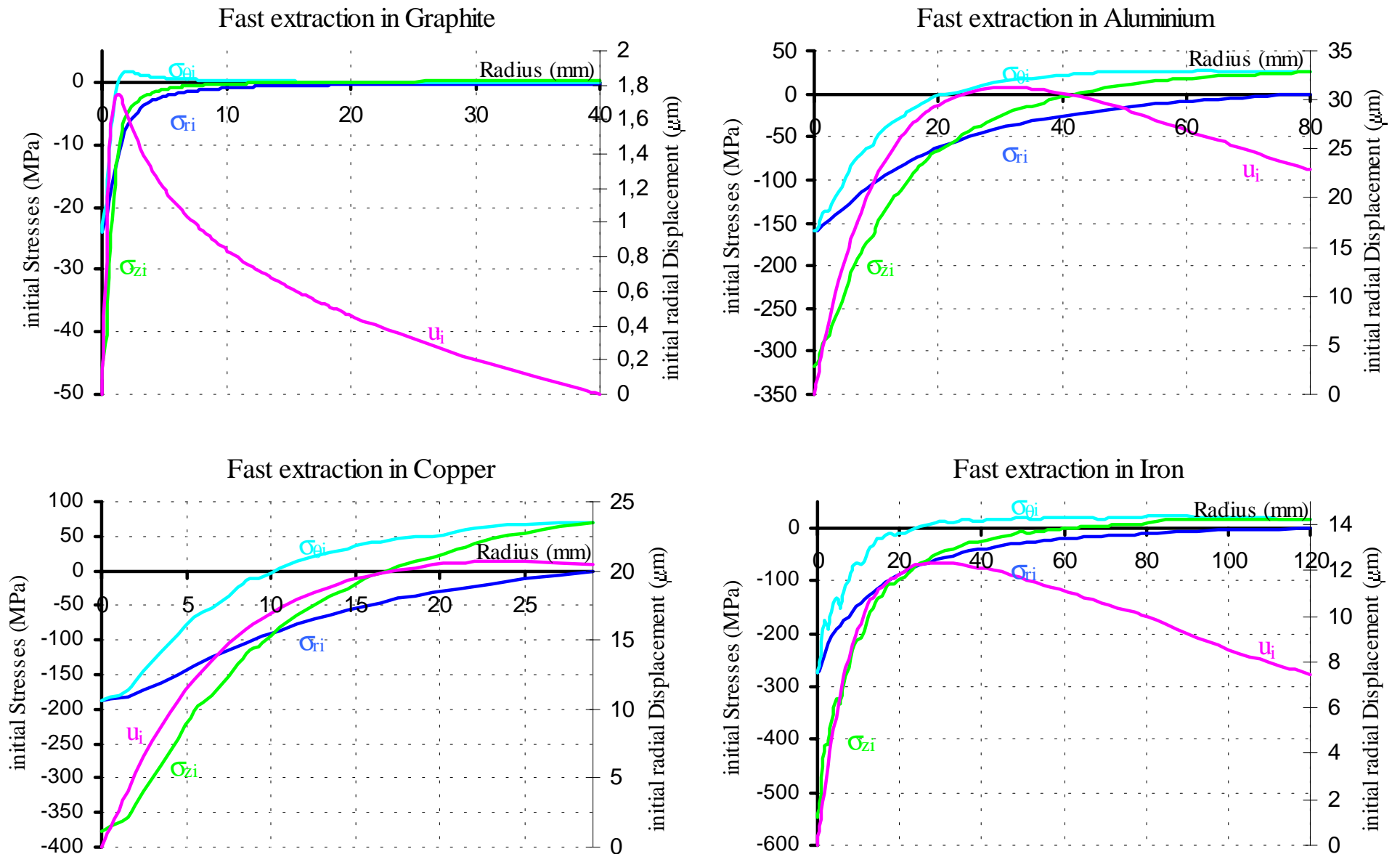
Figure 22 : Initial distribution of principal stresses and radial displacement generated by a 6μs pulse of 5 10^{13} protons.
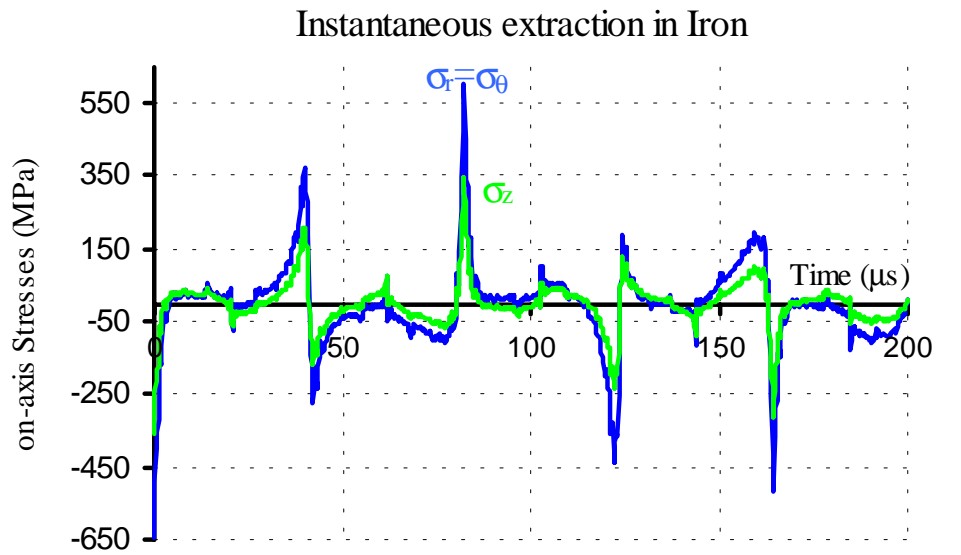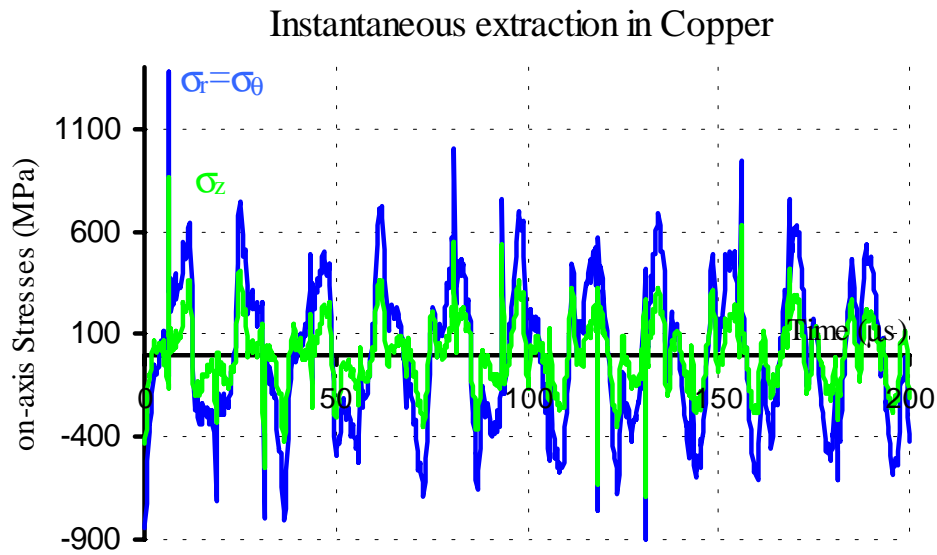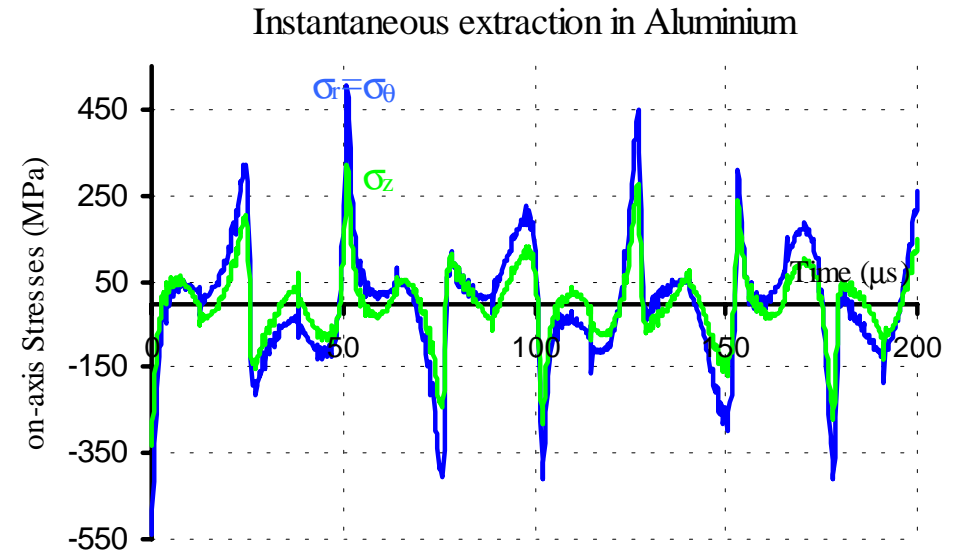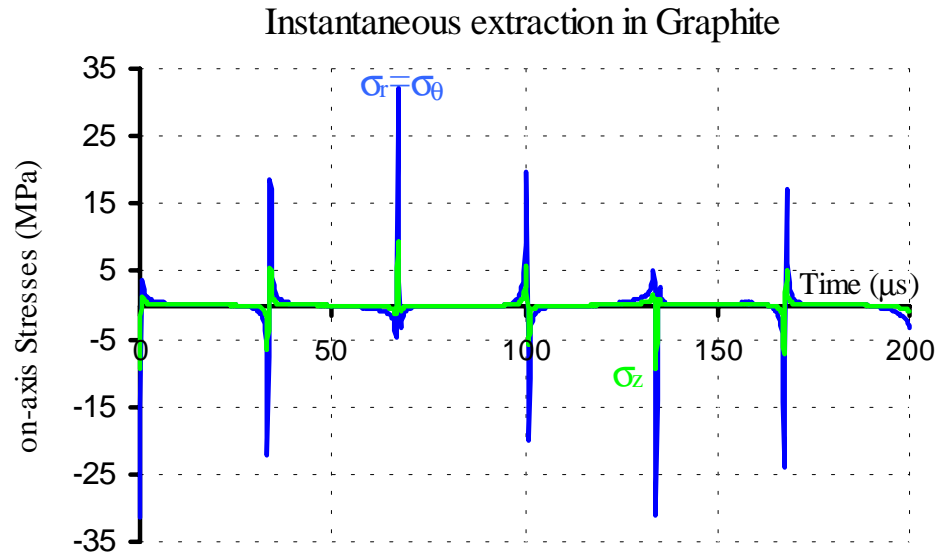
Figure 23 : Time evolution of the principal dynamic stresses generated on-axis by an instantaneous pulse of 5 10[13] protons.

47
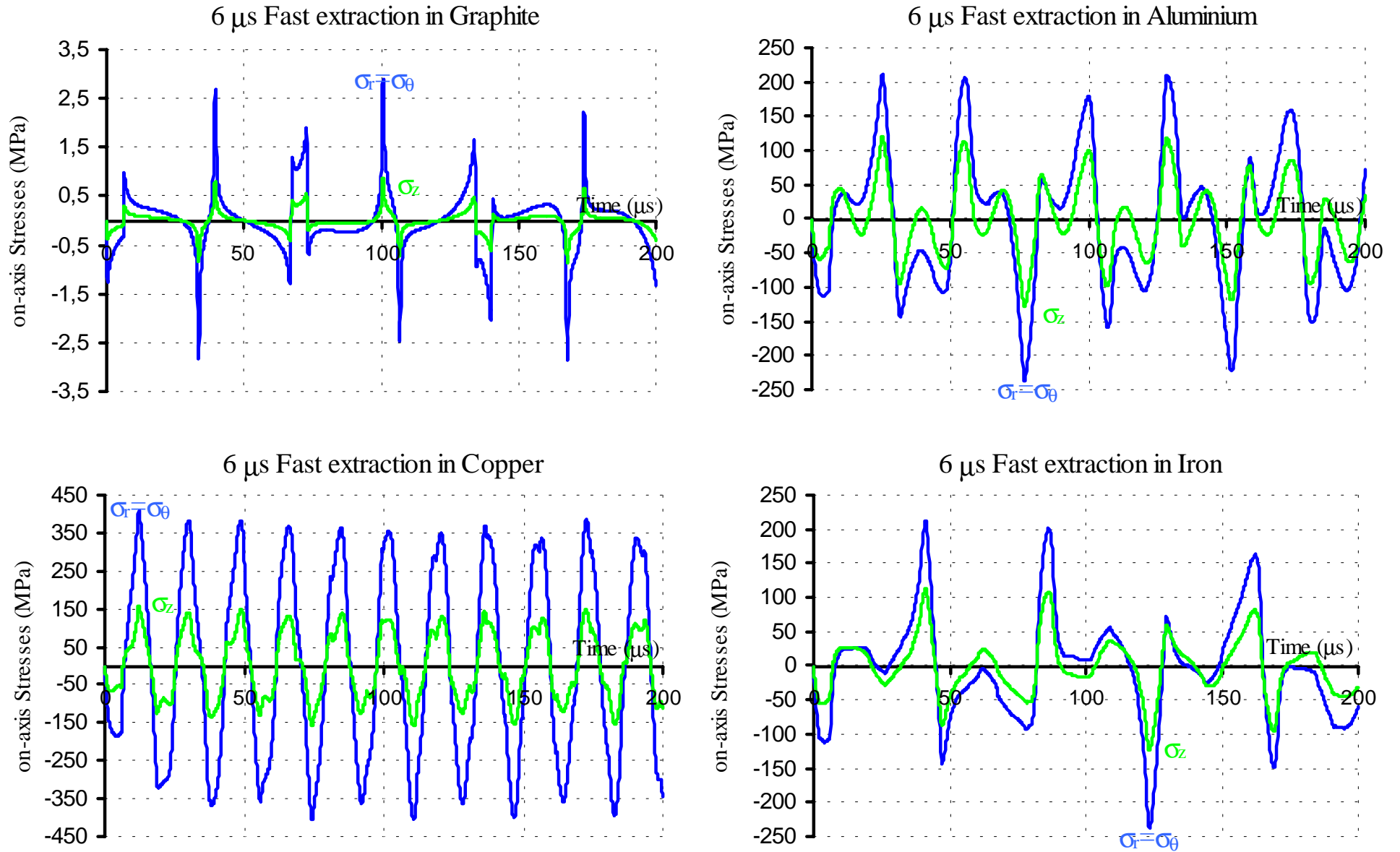
Figure 24 : Time evolution of the principal dynamic stresses generated on-axis by a 6 μs pulse of 5 10^{13} protons.
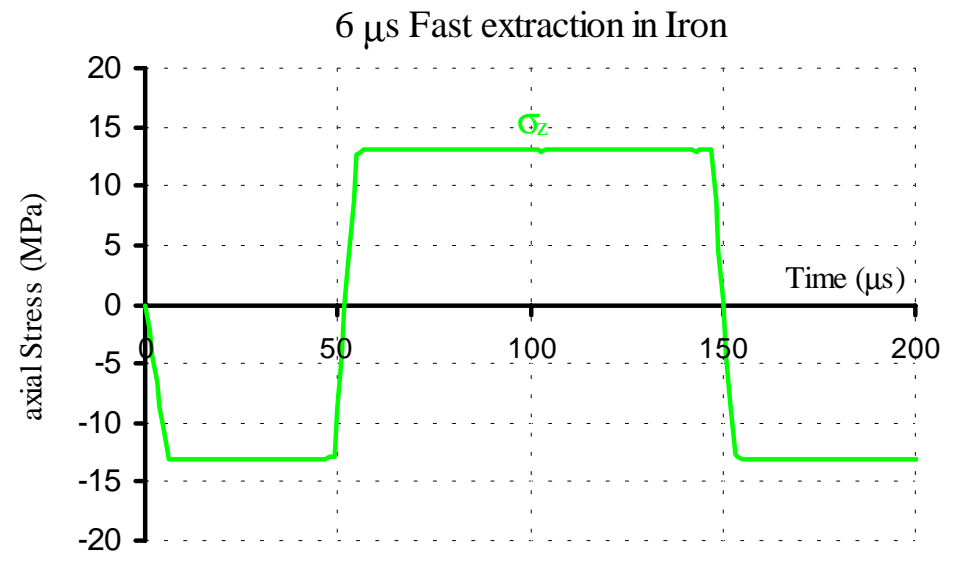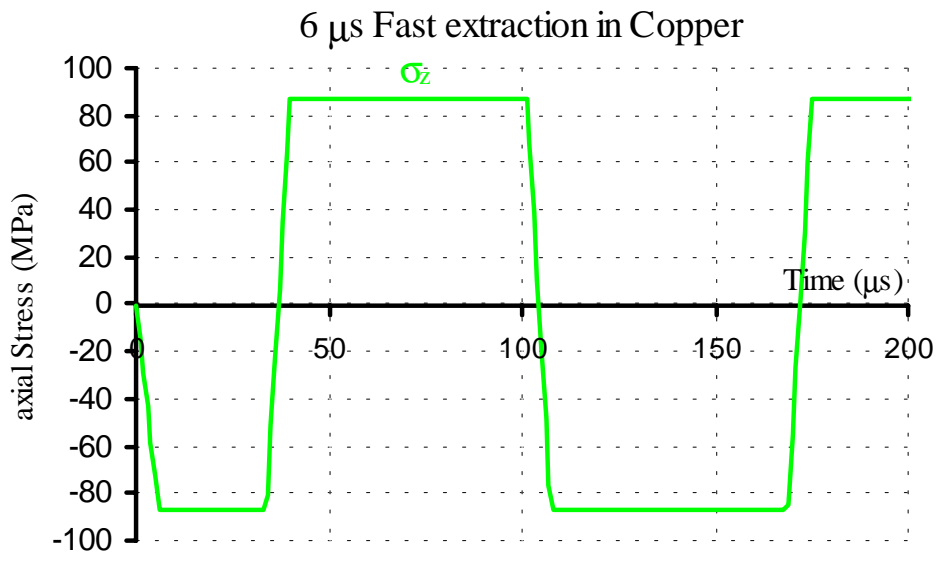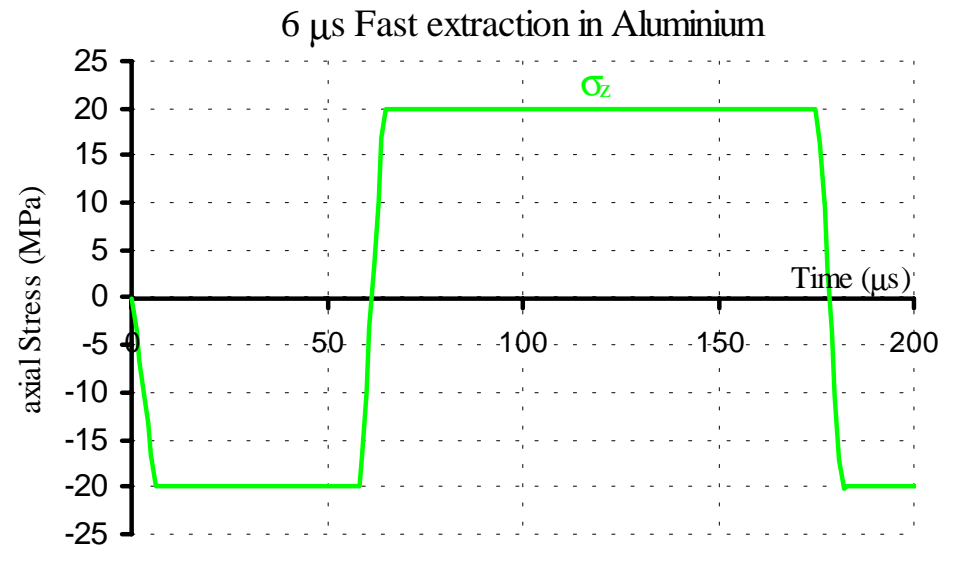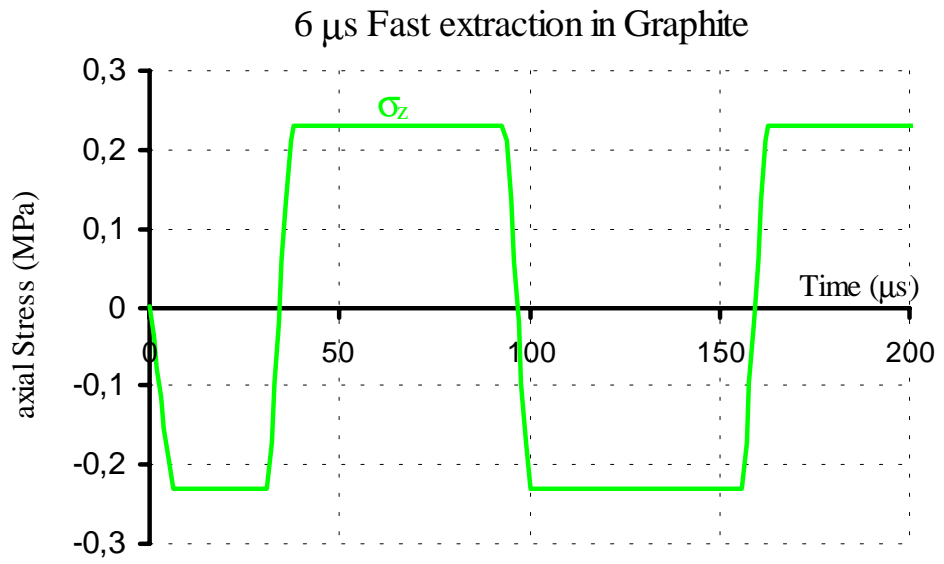
Figure 25 : Time evolution of the axial dynamic stress generated in the middle of the bar by a 6 μs pulse of 5 10^{13} protons.
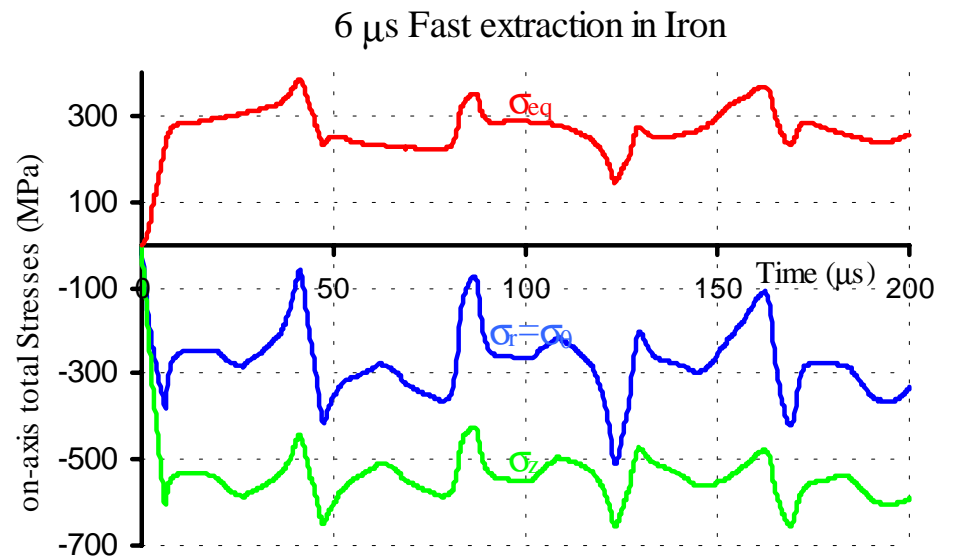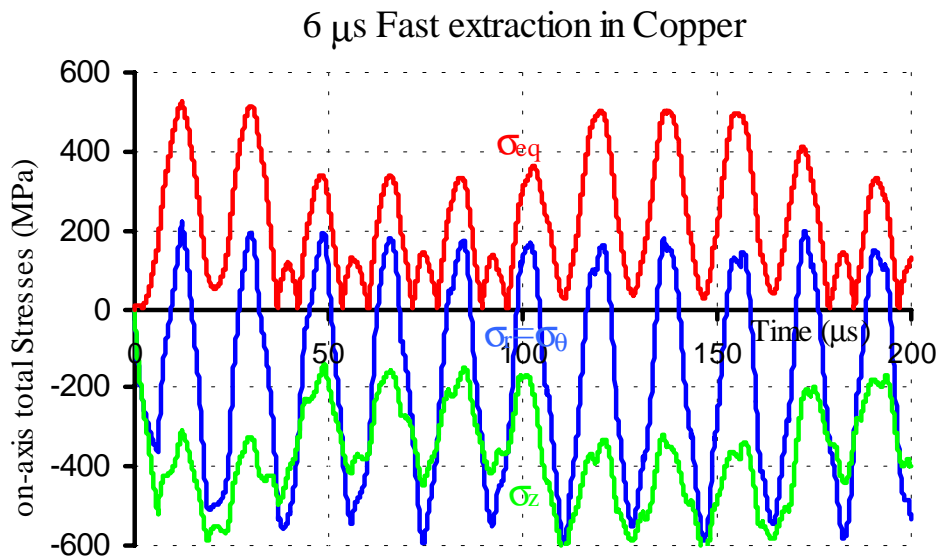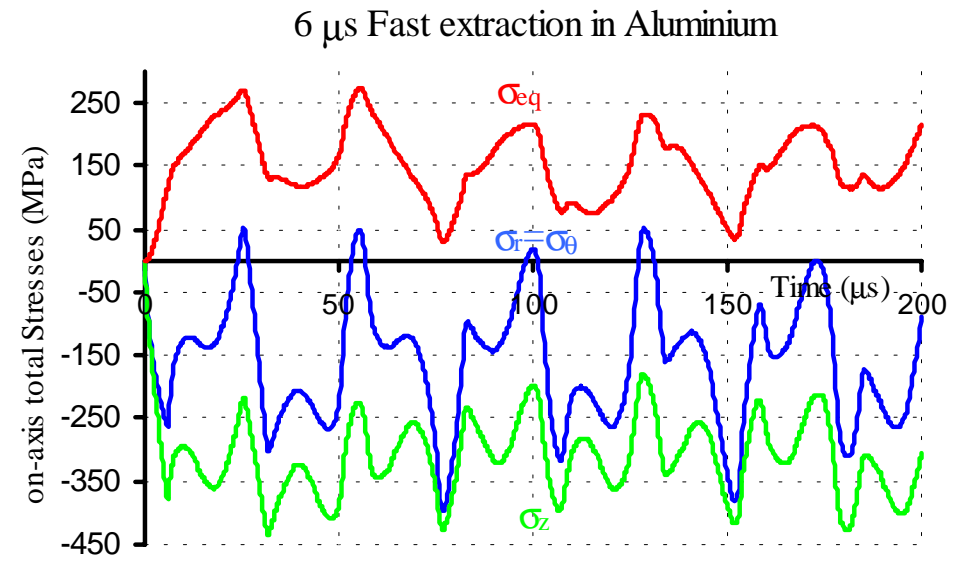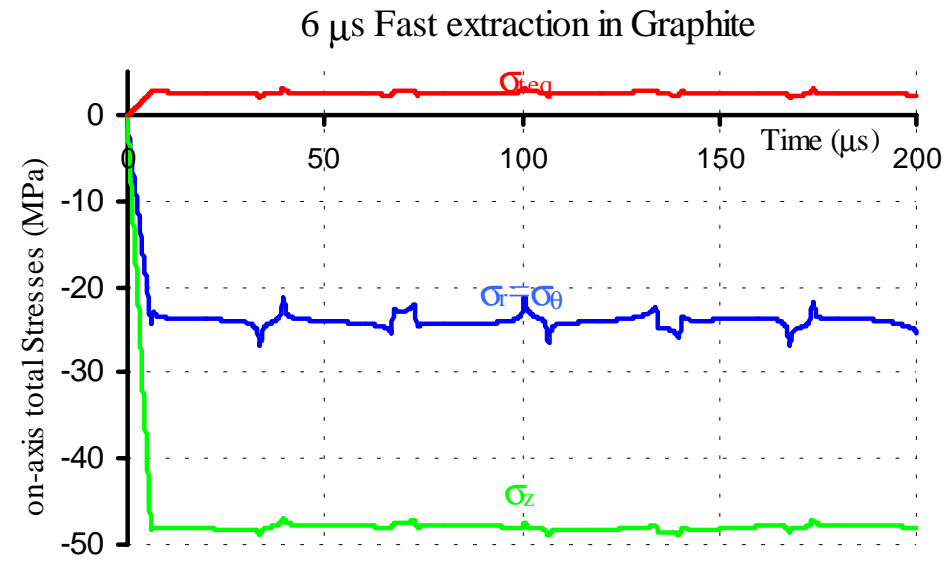
Figure 26 : Time evolution of the total stresses generated at the centre of the cylinder by a 6 μs pulse of 5 10^{13} protons.
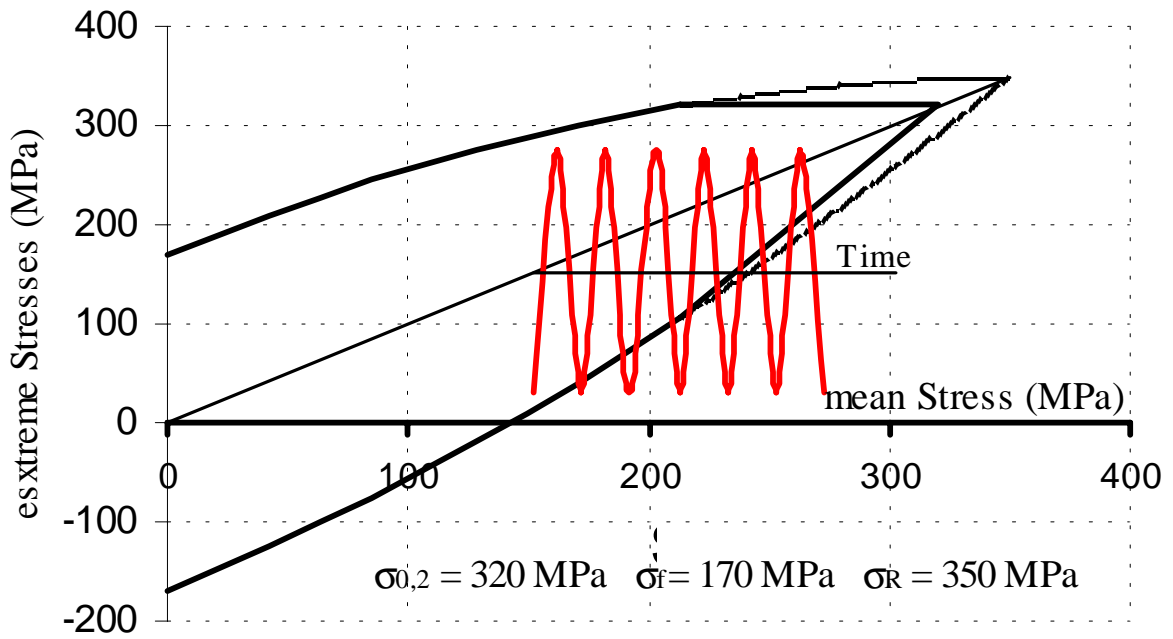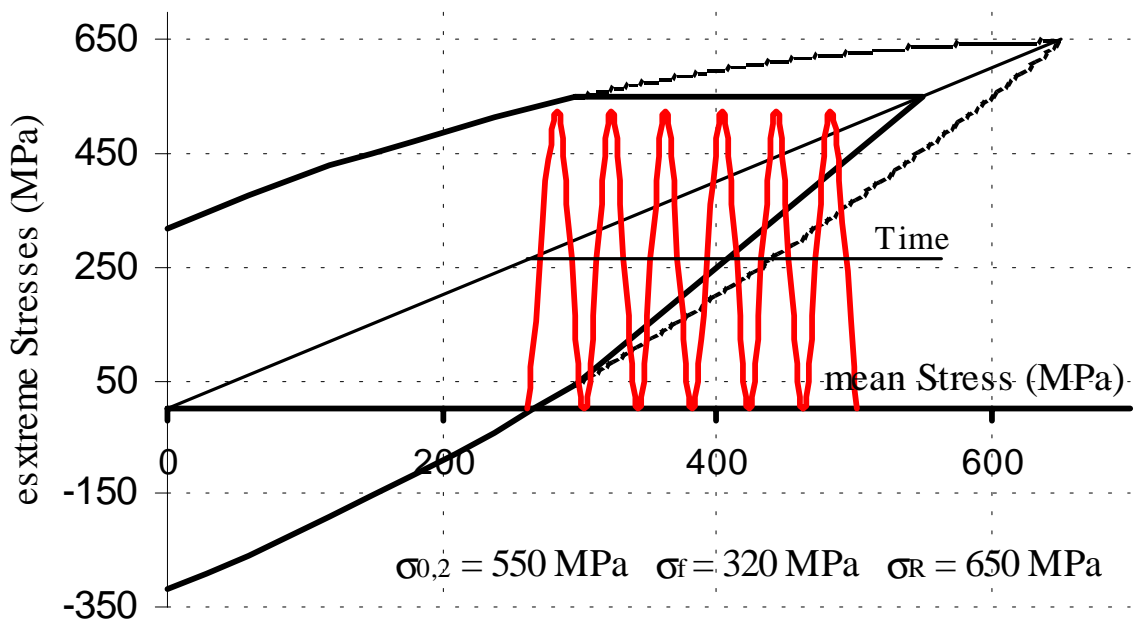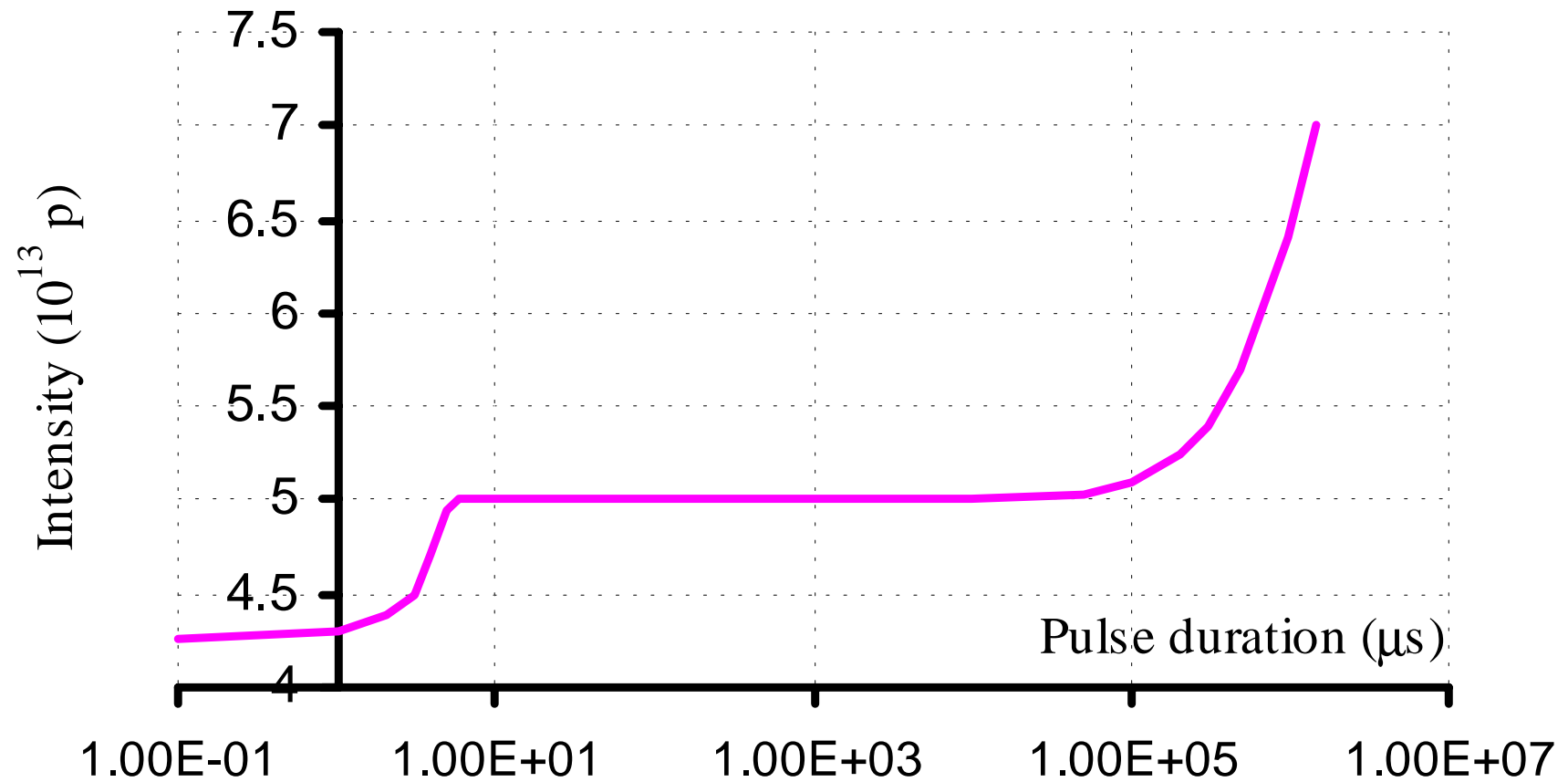
Figure 27 : Goodmann's charts of aluminium and copper alloys.

Figure 28 : Maximum allowed intensity of a 450 GeV beam of radial size 0.58 mm, dumped every 16.8 s.
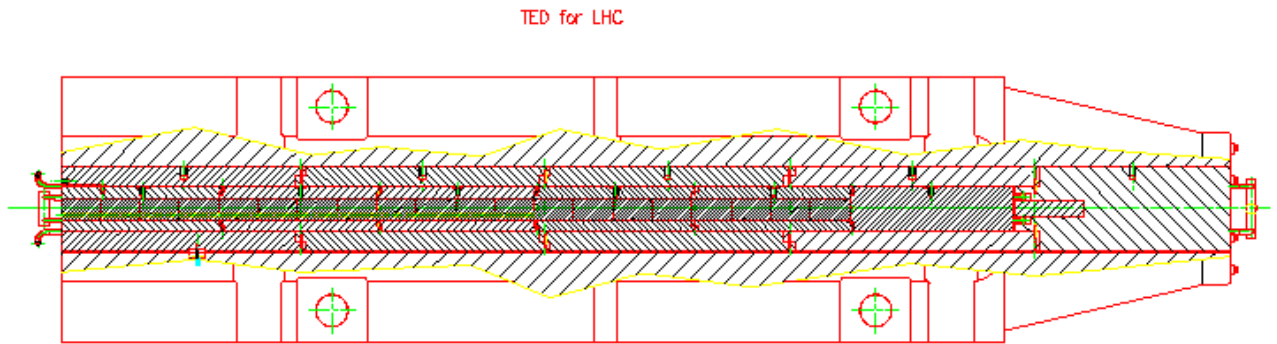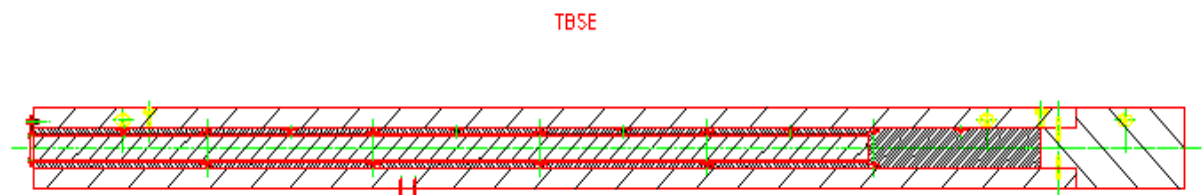
Figure 29 : Side view of the new TED.

Figure 30 : Side view of the new TBSE.